
MASTER'S THESIS

MULTIPATH PROPAGATION IN TIME-OF-FLIGHT 3D-IMAGING

conducted at the
Signal Processing and Speech Communications Laboratory
Graz University of Technology, Austria

in co-operation with
Infineon Technologies Austria AG
Graz, Austria

by

Jakob Mangelberger

Supervisors:
Dipl.-Ing. Dr. Christoph Steiner
Dipl.-Ing. Dr. Thomas Thurner

Assessor:
Assoc.Prof. Dipl.-Ing. Dr. Klaus Witrisal

Graz, June 7, 2018

Statutory Declaration

I declare that I have authored this thesis independently, that I have not used other than the declared sources/resources, and that I have explicitly marked all material which has been quoted either literally or by content from the used sources.

date

(signature)

Abstract

Time-of-flight (ToF) is an imaging technology that uses the propagation delay of reflected light to reconstruct the 3D depth image of a scene. ToF sensors become increasingly available in smartphones and automotive applications due to advantages in size and reduced post-processing requirements w.r.t. other 3D imaging technologies. With extensive calibration effort, a high accuracy on the depth image can be achieved, reducing all major error sources. An additional error source is multipath interference caused by additional return components in the received reflected light. This error cannot be calibrated as it is dependent on the scene and thus needs to be addressed using other means.

Simulations in this thesis, based on a simple multipath channel model, show that the impact of multipath components on the result of the depth measurement which can be substantial under certain scene configurations. These results are validated with measurements from a state-of-the-art ToF camera with amplitude-modulated continuous wave signals. Several scenarios are shown to produce multipath interference. The scenarios cover the effect of mixed pixels (flying pixels between foreground object and background), multi-bounce reflections and scattering in the camera optics, all of which may be present throughout any common image capture.

To reduce the error caused by multipath interference, three algorithms are implemented, based on a multi-frequency approach, this means multiple images are captured at different frequencies of the illumination signal. Two of the algorithms used are from the area of non-linear approximation (separable non-linear least squares) and spectral estimation (MUSIC). Additionally, a simple linear approximation calculation is proposed. The performance of the algorithms is simulated on the error data obtained by the multipath model and the results are validated for MUSIC and linear approximation on real image data for a scene with mixed pixel interference. The results show that both algorithms are able to remove mixed pixel interference, but only work for sufficiently large distance between objects and high enough modulation frequencies.

Zusammenfassung

Time-of-flight (ToF) ist eine Bildaufnahmetechnik, die das 3D Tiefenbild einer Szene mit Hilfe der gemessenen Laufzeit von reflektiertem Licht aufnehmen kann. ToF Sensoren werden immer häufiger in Smartphones und Automotive-Applikationen verwendet, unter anderem wegen ihrer Vorteile bzgl. Größe und geringerem Aufwand in der Bildverarbeitung, verglichen mit anderen Technologien. Eine hohe Genauigkeit in den Tiefendaten kann mit Hilfe aufwändiger Kalibrationsmaßnahmen sichergestellt werden, die die größten Fehlerquellen kompensieren. Eine zusätzliche Fehlerquelle ist die Mehrwege-Interferenz, die durch zusätzliche Komponenten des reflektierten Lichtsignals entsteht. Dieser Fehler ist abhängig von der Zusammensetzung der Szene. Dadurch kann dieser Fehler nicht allgemein kalibriert werden und muss speziell betrachtet werden.

Simulationen in dieser Arbeit zeigen, basierend auf einem einfachem Mehrweg-Kanalmodell, dass der Einfluss von Mehrweg-Komponenten auf das Ergebnis der Tiefenmessung erheblich sein kann. Diese Simulationsergebnisse werden gestützt durch Messungen mit einem modernen ToF Sensor basierend auf amplitudenmodulierten, kontinuierlichen Beleuchtungssignalen. Mehrere Szenarien zeigen die Auswirkungen von Störungen durch Mehrwegeausbreitung. Diese Störungen beinhalten den Effekt von gemischten Pixeln ("fliegende Pixel") zwischen Vorder- und Hintergrund, Reflexionen von anderen Objekten und Streuung innerhalb der Kameraoptik. Alle diese Effekte können und werden in einem üblichen Tiefenbild vorhanden sein.

Um den Fehler durch Mehrwegeausbreitung zu verringern, werden drei Algorithmen implementiert. Diese verwenden einen Mehrfrequenz-Ansatz, das bedeutet mehrere Bilder werden bei unterschiedlichen Modulationsfrequenzen der Beleuchtung aufgenommen. Zwei Algorithmen sind aus dem Bereich der nichtlinearen Näherung (Separable non-linear least squares) und Spektralschätzung (MUSIC). Zusätzlich wird ein einfacher linearer Schätzer vorgeschlagen. Die Qualität der Algorithmen wird mittels Simulation validiert und anschließend auf realen Bilddaten für eine Szene mit gemischten Pixeln nachgestellt. Die Ergebnisse zeigen, dass beide Algorithmen generell das Entfernen von gemischten Pixeln ermöglichen, dies aber nur für ausreichend große Distanzen zwischen den Objekten und ausreichend hohe Modulationsfrequenzen möglich ist.

Nomenclature

ACF	Auto-Correlation Function
AMCW	Amplitude Modulated Continuous Wave
LIDAR	Light detection and ranging
LOS	Line-Of-Sight
MPC	Multipath Component
MPI	Multipath Interference
MUSIC	Multiple Signal Classification
PMD	Photonic Mixer Device
SNLLS	Separable Non-Linear Least Squares
SNR	Signal-to-Noise Ratio
SRF	Sensor Response Function
ToF	Time-of-flight
VCSEL	Vertical-cavity surface-emitting laser

Contents

1	Introduction	1
1.1	About this thesis	1
2	Time-of-Flight Basics	3
2.1	ToF principle	3
2.1.1	Photonic Mixer Device	4
2.1.2	Advantages of ToF	5
2.2	Error Sources	5
2.2.1	Systematic Errors	5
2.2.2	Statistical Errors	7
3	Signal Processing Framework	8
3.1	Signal Path Model	8
3.1.1	System Overview	8
3.2	Sensor Response Function	9
3.2.1	Derivation	10
3.2.2	Basic Properties of the SRF	11
3.3	Distance Estimation	11
3.3.1	Correlation Function Analysis	12
3.3.2	Fourier method	13
4	Multipath Propagation in ToF	15
4.1	Introduction to Multipath Propagation	15
4.2	Sources for Multipath Propagation in ToF Imaging	15
4.3	Modeling Multiple Returns	17
4.4	Multipath Signal Model	18
4.4.1	Sensor Response Function in MPI	18
4.4.2	Distance estimation in MPI	18
4.4.3	Phasor representation of multipath components	19
5	Multipath Interference Compensation	23
5.1	Introduction to MPI	23
5.1.1	MPI as channel estimation problem	23
5.2	Intra-Scene Reflection Modeling	24
5.3	Multifrequency Compensation	24
5.3.1	Nonlinear Regression	25
5.3.2	Spectral Estimation	26
5.3.3	Linear Regression	26
5.4	Correlation Waveform Deconvolution	27
6	Simulations and Experiments	29
6.1	Simulation Framework	29

6.2	Measurement Setup	29
6.2.1	Setup Overview	29
6.2.2	Calibration	30
6.2.3	Measurement Scenarios	32
6.3	Simulation of Multiple Returns	33
6.3.1	Single Multipath Return	33
6.3.2	Multifrequency Return	36
6.3.3	Simulated MPI Compensation	37
6.3.4	Frequency dependency	39
6.3.5	Additional MPCs	40
6.4	MPI in Practice	42
6.4.1	Intra-Scene Reflections	42
6.4.2	Mixed Pixels	43
6.4.3	Scattering	46
6.5	MPI Compensation	48
6.5.1	Choosing the correct frequency	49
6.5.2	Mixed Pixels with insufficient distance	51
7	Conclusion	53
7.1	Summary	53
7.1.1	Multipath Error	53
7.1.2	Multipath Compensation	53
7.2	Outlook	54

Introduction

Time-of-flight 3D Imaging, as well as other imaging technologies like structured light or stereoscopy enjoy increasing popularity in consumer, automotive and home applications. Applications include augmented reality or face recognition in smartphones, gesture control and cabin monitoring in cars and surveillance systems for home security. The Time-of-flight (ToF) imaging technology uses direct or indirect information on the actual travel time of an illumination signal from sender to receiver. One option is the direct measurement of time-of-flight by precise timing between sending and receiving station which is used e.g. in Lidar applications. This thesis specifically focuses on Amplitude Modulated Continuous Wave (AMCW) Time-of-Flight imaging. The technology uses single-frequency periodic light illumination for an indirect correlation-based approach with a Photonic Mixer Device.

As with all methods involving wave propagation, the receiving station has to always deal with effects of multipath (similar as in radar, mobile communications, etc...). Multipath propagation is well understood for RF communications and can be extended partly into the ToF context. ToF additionally suffers from effects specific to its optical signal (e.g. mixed pixel and scattering).

Only a few papers are exploring the problem of multipath interference (MPI) in AMCW Time-of-flight systems on a signal level. First approaches consider a radiometric model to calculate possible multipath interference in single scene images [1] [2]. This requires detailed knowledge of the scene and is expensive in calculation. Other multipath models base the calculation of MPI on multiple image captures. Godbaz et. al. [3] have shown the existence of a closed-form inverse solution for the multipath problem limited to a return with two components. Closed form solutions have not been proposed for more than two components, here the solutions generally require estimation algorithms for an approximate solution. Later publications [4] show the reconstruction of multiple multipath components using a sequence of equally spaced modulation frequency measurements and sparse frequency approximation. A fundamentally different approach is proposed by discarding the AMCW modulation scheme and using coded modulation to eliminate the inherent ambiguities in the AMCW ranging scheme [5].

The goal of this thesis is to understand the source and characteristics of MPI in the context of AMCW ToF via simulations and validate the proposed solutions in an experimental setup using a state-of-the-art commercially available 3D imaging camera.

1.1 About this thesis

This thesis is conducted as a collaboration between INFINEON TECHNOLOGIES AUSTRIA AG and the SIGNAL PROCESSING AND SPEECH COMMUNICATION LABORATORY (SPSC) at Graz University of Technology.

The thesis first introduces the basic technology in Chapter 2. It also touches briefly on several errors present aside from the topic of this thesis which need to be considered for an accurate ToF setup. Chapter 3 then defines the specific type of system used in further chapters and introduces

a general framework describing the operation of these basic ToF systems. This is extended to include a multipath propagation model in Chapter 4 and shows the effect of MPI on the imaging result. Based on the framework presented in previous chapters, Chapter 5 expands on several possibilities to compensate the multipath interference present in ToF imaging. Chapter 6 then shows the effects of MPI in an experimental setup and implements and compares compensation methods. The thesis is summarized with its conclusions in Chapter 7.

Time-of-Flight Basics

This chapter introduces the general concept of time-of-flight imaging. Section 2.1 shows the basic idea behind ToF imaging technology for different variants. The technology is also defined by several systemic and statistical error sources with some of them described in Section 2.2.

2.1 ToF principle

Time-of-flight imaging is a 3D imaging technology used to directly acquire depth information. The principle behind Time-of-Flight is fairly simple, basically the goal is to determine the propagation time of light. Given the propagation time of light the distance to a target surface can be derived via

$$d = \frac{1}{2} \cdot c \cdot t_d \quad (2.1)$$

where c is the speed of light ($\approx 3 \cdot 10^8 \frac{m}{s}$ in air) and t_d is the measured time delay between an emitted and reflected light beam. The factor $\frac{1}{2}$ is based on the assumption that light source and sensor position are identical and therefore the light has to travel twice the distance to return to the sensor after being reflected on the target object. Deviations from these assumptions can easily be corrected via necessary calibrations [6].

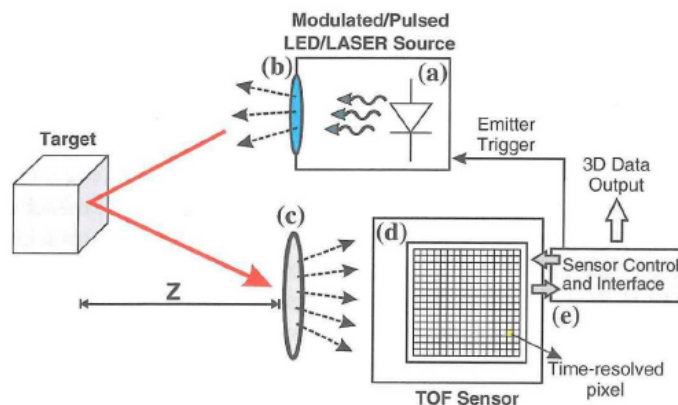


Figure 2.1: General Time-of-Flight detection system [7]

Fig. 2.1 shows a general time-of-flight measurement setup. The scene can be illuminated by either LED or Laser/VCSEL technology (a). The technology and wavelength used might be specific to the application, but in general light in the infrared spectrum is used to limit interference from ambient light and make it unobtrusive. A diffuser (b) might be necessary to illuminate the entire scene as well as an optical lens (c) to gather the reflected light onto the actual ToF sensor area (d).

The setup in Fig. 2.1 does not specify the type of ToF sensor employed. A basic differentiation is into direct and indirect Time-of-Flight. Direct ToF is based on the actual exact measurement of the time delay or phase difference, basically a high time-resolution stopwatch. This time-resolution requirement makes camera designs for direct ToF challenging. Indirect ToF on the other hand indirectly derives the time delay from a time-gated measurement of the received light intensity. Both D-ToF and I-ToF are possible for pulsed or continuously modulated light, measuring time and phase delay respectively.

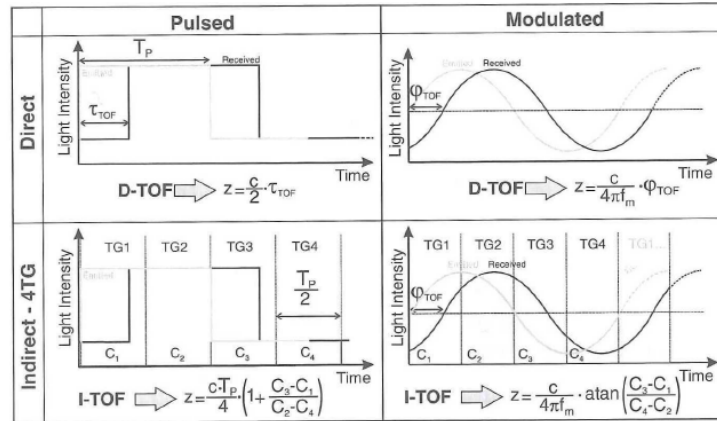


Figure 2.2: Overview of different basic ToF measuring techniques [7]

Fig. 2.2 shows the difference for the D-ToF and I-ToF measuring techniques for simple rectangular pulses and sinusoidal modulated light time-gated at four delays. Both techniques rely on specialized pixel structures to achieve an acceptable performance. D-ToF uses sensors with avalanche photo diodes or single-photon avalanche diodes to measure the time delay down to a resolution of tens of picoseconds [8] while I-ToF achieves high precision using In-Pixel Photonic Mixer Devices.

2.1.1 Photonic Mixer Device

First ToF systems were developed in the 1970s and were used as scanning systems. Only the introduction of devices capable of simultaneous light detection and demodulation in the 90s allowed the development of scannerless range cameras [9]. This Photonic Mixer Device (PMD), also often called a lock-in pixel, demodulation pixel or correlation pixel, allows for the compact design of the sensor in standard CMOS or CID technologies by inherently performing the mixing of incoming optical and electrical reference signal. A prototype based on this pixel design was first realized in [10].

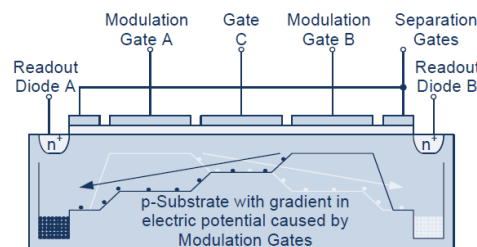


Figure 2.3: PMD Pixel Schematic (Source: Infineon Technologies Austria AG)

Fig. 2.3 shows the general design of a single PMD pixel. On the light-sensitive layer of the pixel, the inner photoelectric effects splits the incident photons into electron-hole pairs. The generated electrons are then driven towards the read-out nodes using a potential profile determined by the

modulation gate A/B electrodes. Depending on the potential difference of the gate electrodes the electrons gather into single so-called buckets at Readout Diode A/B, that can be read out after certain integration intervals.

The charge in the buckets is proportional to the time the optical signal is arriving on the sensor and the gate voltage direction. A readout will be at a maximum if the optical signal is equal to the gate voltage, since all incoming light will fill the respective bucket. If the optical signal is the exact opposite then the same bucket will be mostly empty while the opposite bucket will contain the generated charges. Therefore the mixing done in the pixel can be simplified as a correlation over the integration interval.

2.1.2 Advantages of ToF

The following list shows some benefits of ToF compared to other 3D imaging technologies:

- Depth is the direct result of the measurement. No additional algorithmic effort (e.g. feature extraction)
- Independent of scene texture
- No moving parts required (compared to scanning technologies)
- High framerate through parallel measurement on all pixel
- Compact form factor

Some advantages are valid in comparison to other technologies but might still be comparable or worse to others. E.g. the form factor is relatively small compared to stereoscopic methods due to its requirements on a certain baseline distance. On the other hand methods based on normal imaging cameras (e.g. structured light) will achieve a higher pixel density due to generally smaller pixel size. The PMD pixel design does allow for fast and simple depth calculation but requires more space than conventional pixels, leading to overall lower resolution on PMD based cameras. Also, while independent of scene texture, the linear dependency to light of the PMD pixel causes dynamic range issues [11], where the effective range for a specific light power is significantly lower than for conventional pixel designs.

2.2 Error Sources

ToF systems suffer from a variety of systematic and statistical errors. Some are strongly dependent on the actual sensor implementation, others are valid for all systems. The following points represent a sample of the errors which are responsible for a majority of the distance deviation introduced in a ToF system.

2.2.1 Systematic Errors

Circular Distance Error

Also called Wiggling Error, this error is specific to AMCW ToF systems and is caused by an incorrect estimation of the distance due to non-sinusoidal waveforms used in illumination. The error can be significant and is dependent on the distance to the target object. This distance-dependency makes calibration time-consuming and complex as the calibration needs to be performed to work at all distances.

This error has been investigated in detail [11]. Fig. 2.4 shows the Wiggling Error for different integration times and its dependency of the real target distance.

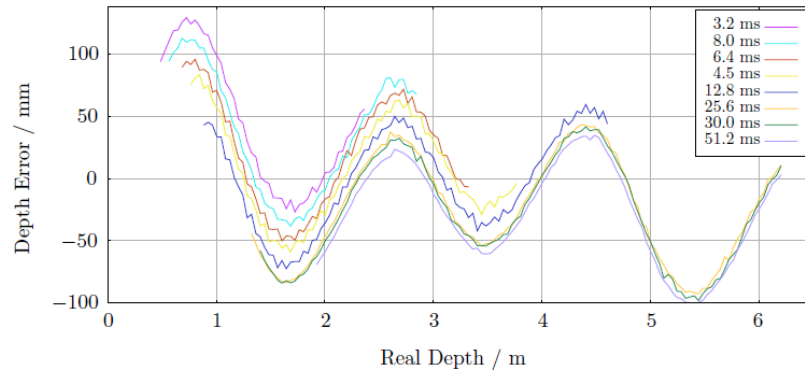


Figure 2.4: Wiggling Error for different integration times [11]

Intensity-related Error

This error (also called amplitude-related error) describes a distance offset caused by different reflective properties of the target surface. Therefore light areas are measured at a different distance as dark areas. This problem can also be dealt with calibration [12].

Time-related Error

Integration time has also an influence on the distance error. The error is constant over distance which allows for simple calibration. High integration times are advantageous for SNR and are therefore favorable. For the PMD pixel specifically this might be caused by asymmetric charge separation in the pixel which causes increased errors with increasing integration time.

Fixed Pattern Noise

FPN is caused by differences of individual pixel or mismatch in their readout. This is specific for each product and for each individual sensor chip. This cannot be described analytically or predicted and needs to be calibrated, most simply by generating a look-up table over the complete sensor array.

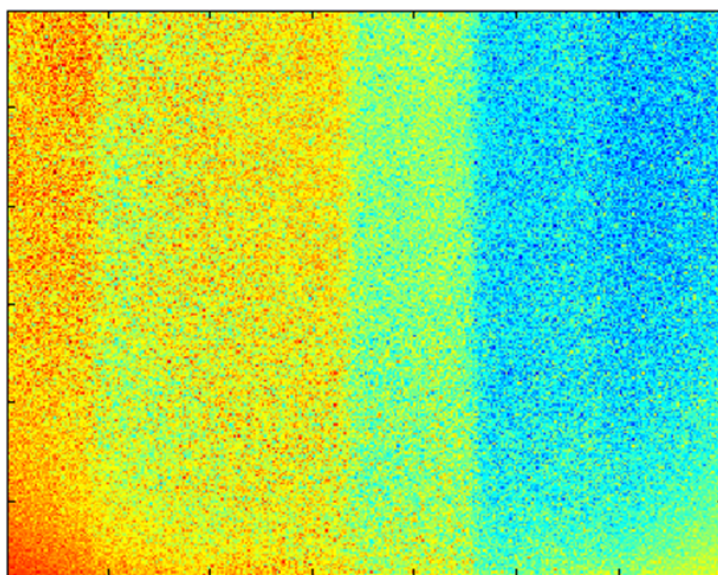


Figure 2.5: Raw reset image readout for the IRS1125C

Fig. 2.5 shows a raw image readout for the Infineon IRS1125C chip used in Chapter 6. The image is taken without light or integration time and therefore shows the inherent difference between the different pixels caused by mismatch in readout (column effect) and pixel supply for a single frame.

Multipath Error

In contrast to the other errors in this section, multipath interference cannot be mitigated using calibration as the error is strictly scene dependent. Details follow in Chapter 4.

2.2.2 Statistical Errors

Photon Shot Noise

Photon Shot Noise is dependent on the number of photons incident on the pixel. The generated noise is dominant especially for low temperatures and follows a Poisson distribution with the number of photons. PSN can be reduced by higher integration times or lower illumination power.

Additionally to shot noise caused by photons, there is also shot noise generated by photo diode leakage current, which is often called *Dark Shot Noise*.

kT/C Noise

Additional noise is generated by the electronic noise generated by the thermal agitation of charge carriers. For optical sensors this typically concerns the readout capacitor, which generates reset noise [13]. This noise is independent of the signal intensity, contrary to PSN.

Quantization Noise

Analog-digital conversion of the resulting pixel voltage cannot be done in infinitely small resolution. Difference of conversion value to real value causes noise in the resulting digitized value. This can be avoided by adequately high resolution to force the quantization noise below the other noise sources (PSN or kT/C).

Signal Processing Framework

This chapter focuses on establishing a mathematical framework for a general ToF imaging system. Most components are idealized to keep the model as simple as possible while providing the necessary complexity to explore the properties of the ToF system used throughout this thesis. Section 3.1 introduces a system path model that is more detailed in Section 3.2. The outcome is the definition of the sensor response function (SRF) that allows the distance estimation in Section 3.3.

3.1 Signal Path Model

3.1.1 System Overview

Fig. 3.1 shows a general system overview for the signal path of a simple ToF system.

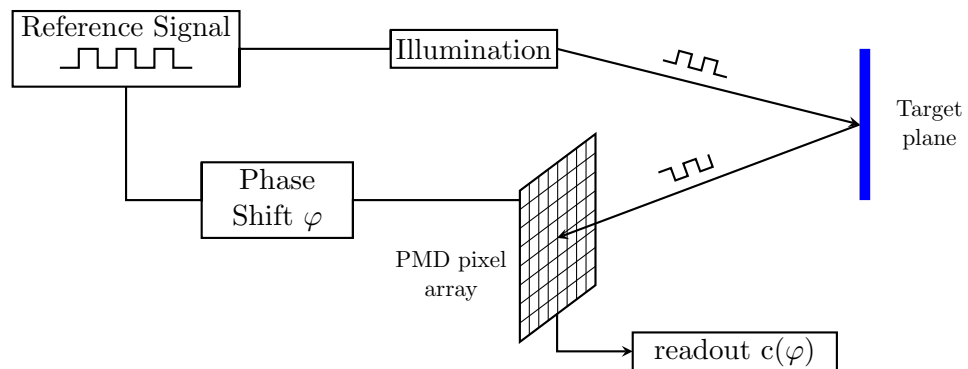


Figure 3.1: Block diagram of the signal path for a continuous wave ToF system.

The block diagram shows the function for a general indirect ToF system using a Photonic Mixer Device and a rectangular waveform as reference signal (as is used in the experimental setup). For a general ToF system there are no restrictions towards the form and periodicity of the illumination signal, for AMCW Lidar the reference signal is a single frequency waveform. The reference drives an illumination system which reflects light off the target plane or target object. The reflected light is captured by the pixel generating a signal related to the target distance. The output $c(\varphi)$ of the model is a single integration period of the sensor pixel, and thus a single value of the correlation function between the reference and the optical signal at a specific shift φ . The phase delay introduced in the sensor path¹ is therefore used to sample the correlation function at different time lags.

As stated in Section 2.1 this is not the only possible realization of a time-of-flight system. This model is chosen as it is used in current commercial implementations and research and also

¹ Can also be introduced in the illumination path or both paths simultaneously. More complex pixel with multiple shutters can also make direct phase shifting unnecessary [14].

available as an experimental setup for this thesis.

3.2 Sensor Response Function

The signal flow graph for the ToF system under consideration is shown in Fig. 3.2. All considered components from Fig. 3.1 are now replaced by their corresponding impulse responses and the PMD pixel as a simple correlation model. The input is the reference signal $r(t)$ and the output $c(\varphi)$ is the correlation value at a specific phase shift φ .

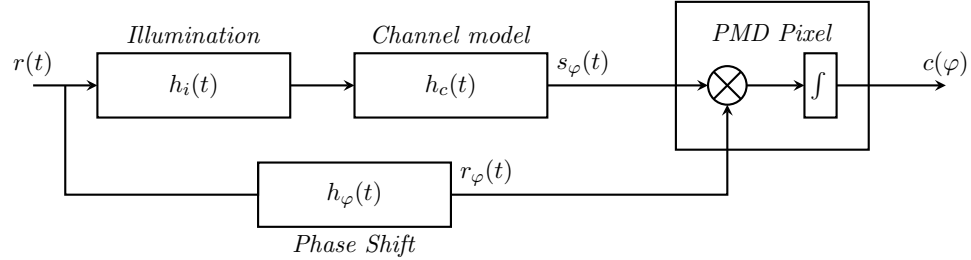


Figure 3.2: Signal flow graph for the AMCW ToF System

Phase Shift

The phase shift is responsible for a variable time shift of the reference signal $r(t)$.

$$h_{\varphi}(t) = \delta\left(t - \frac{\varphi}{2\pi f}\right) \quad (3.1)$$

The range and resolution selectable for φ defines the possible distance estimation algorithms as well as modulation frequencies. If φ is derived from the illumination signal period arbitrary modulation frequencies are possible. This is the assumption here with $\varphi = [0, 2\pi)$ and f being the modulation frequency of the reference signal.

Illumination

The illumination of the scene can theoretically be any light source to create a response on the sensor. Usually the light is non-visible in the infrared spectrum and is created using LEDs or Laser diodes. Especially for LEDs the transfer function usually shows significant lowpass characteristics already at low frequencies.

For the following derivation the illumination source is assumed ideal, which means a perfect production of the reference signal. For the impulse response this is represented by a single non-delayed Dirac delta function.

$$h_i(t) = \delta(t) \quad (3.2)$$

Optical Path

In the case of a single reflection in the scene (no multipath returns) the impulse response can simply be described as the impulse response for a linear time invariant channel with a single attenuated delay.

$$h_o(t) = g(d) \cdot \delta(t - t_d) \quad (3.3)$$

t_d is the time delay introduced by the optical path and $g(d)$ is the attenuation caused by the distance traveled and the reflection off the target surface.

3.2.1 Derivation

Using the impulse responses and simplifications in Section 3.2 we now derive the result for the SRF $c(\varphi)$ of the imaging system defined in Section 3.1.

As modeled in Fig. 3.2 the sensor pixel can be approximated as the correlation of the reference signal $r(t)$ and the received signal $s_\varphi(t)$,

$$c(\varphi) = \int_0^\tau s_\varphi(t) \cdot r(t) dt \quad (3.4)$$

where τ is the integration time of the pixel. To be correct it is necessary for the correlation to be performed over an integer multiple of periods of the reference signal. Given the integration period over full periods we can also assume, without loss of generality, the integration start to be at zero.

The optical path is easily described as the convolution of its individual impulse responses. The impulse response of the illumination is a simple Dirac delta function and a neutral element under the convolution. Using its shifting property the shifted Dirac delta function results simply in a delay of the input signal. Using these two properties we can simply calculate the received signal as a scaled and shifted version of the reference signal.

$$s_\varphi(t) = h_\varphi(t) * h_i(t) * h_c(t) * r(t) \quad (3.5)$$

$$\begin{aligned} s_\varphi(t) &= \delta\left(t - \frac{\varphi}{2\pi f}\right) * \delta(t) * [g(d) \cdot \delta(t - t_d)] * r(t) \\ &= \delta\left(t - \frac{\varphi}{2\pi f}\right) * g(d) \cdot r(t - t_d) \\ &= g(d) \cdot r\left(t - t_d - \frac{\varphi}{2\pi f}\right) \end{aligned} \quad (3.6)$$

Using (3.6) in (3.4)

$$c(\varphi) = g(d) \int_0^\tau r\left(t - t_d - \frac{\varphi}{2\pi f}\right) \cdot r(t) dt \quad (3.7)$$

we have a complete expression for the Sensor Response Function. The SRF in (3.7) is now equivalent to the auto-correlation of the reference signal $r(t)$ for an offset of $-t_d$. For any real-valued function the auto-correlation has its maximum value with its quadratic average at zero lag. Given the offset, the maximum of $c(\varphi)$ has to be at a phase delay equal to a time-lag of t_d .

Given the correlation function for $c(\varphi)$, if we can find

$$\varphi_d = -\arg \max_{\varphi} \{c(\varphi)\} \quad (3.8)$$

we know the time delay of the optical path with

$$t_d \stackrel{!}{=} \frac{\varphi}{2\pi f} \quad (3.9)$$

From (2.1) we then can calculate the distance responsible for the measured time delay.

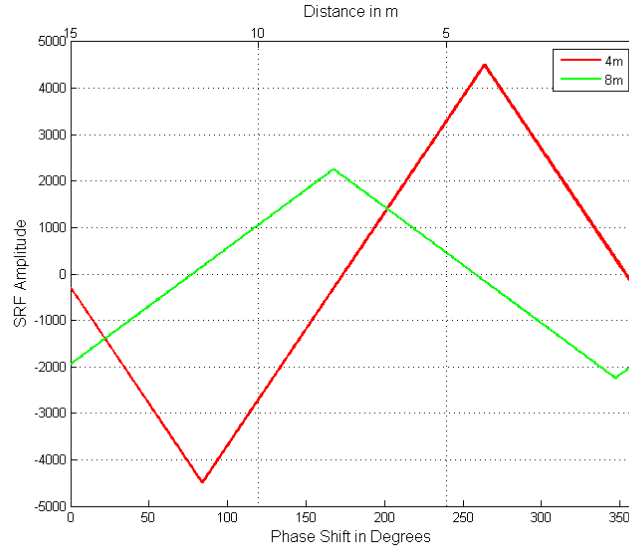


Figure 3.3: Sensor response function example at two different distances.

Fig. 3.3 shows the SRF calculated at two different phase delays equivalent to 4m and 8m respectively given a rectangular reference signal at a modulation frequency of 10MHz.

3.2.2 Basic Properties of the SRF

The SRF shape is defined by the correlation property of the PMD pixel and the phase delay introduced by the various system blocks. Given an ideal periodic reference signal the SRF is:

- Periodic
- Non-zero offset
- Shifted relative to t_d

The shape can be easily predicted given the correlation. E.g. a rectangular reference signal will create a triangular SRF (Fig. 3.3), a sinusoidal reference signal will again create a sinusoidal SRF.

3.3 Distance Estimation

The result for any ToF Measurement is the distance to a target object. As seen in the previous section the phase delay caused by the distance can be found with the maximum argument of the Sensor Response Function (3.8). Obviously that would be exactly possible using an exhaustive search over the finely resolved SRF but this is practically not feasible, both from a limited resolution of the phase shifter and the time necessary to perform enough measurements.

Following, two possible distance estimations for AMCW ToF systems are derived in the time domain, using the definition for the correlation, and in the Fourier domain.

3.3.1 Correlation Function Analysis

For the derivation the theoretical definition of the cross correlation is used.

$$c(\tau) = \int_0^T r(t)s_{\varphi}(t - \tau)dt \quad (3.10)$$

The sign of the lag in (3.10) is different from the usual definition to be consistent with (3.7). Additionally the reference signal is assumed to be sinusoidal with

$$r(t) = \cos(\omega t) \quad (3.11)$$

where $\omega = 2\pi f$ with f being the modulation frequency. Consequently the received signal is

$$s(t) = a \cdot \cos(\omega t - \varphi_d) \quad (3.12)$$

With reference signal and received signal put into (3.10) we can derive the theoretical result of the cross correlation by using trigonometric calculus.

$$\begin{aligned} c(\tau) &= \int_0^T \cos(\omega t) \cdot a \cdot \cos(\omega(t - \tau) - \varphi_d)dt \\ &= \frac{a}{2} \cdot \cos(\omega\tau - \varphi_d) \end{aligned}$$

In order to determine the parameters $g(d)$ and φ_d we need at least two measurements at different τ . State-of-the-Art distance estimation uses four measurements at $\tau_i = \left[0, \frac{T}{4}, \frac{T}{2}, \frac{3T}{4} \right]$. This estimation is called the *4-Phase algorithm* in this thesis.

$$\begin{aligned} c(\tau_0) &= \frac{a}{2} \cdot \cos(\varphi_d) & c(\tau_1) &= \frac{a}{2} \cdot \sin(\varphi_d) \\ c(\tau_2) &= -\frac{a}{2} \cdot \cos(\varphi_d) & c(\tau_3) &= -\frac{a}{2} \cdot \sin(\varphi_d) \end{aligned}$$

From these four cross correlation results the amplitude a can be computed by

$$a = \frac{1}{2} \sqrt{(c(\tau_3) - c(\tau_1))^2 + (c(\tau_0) - c(\tau_2))^2} \quad (3.13)$$

and the phase by

$$\varphi_d = \text{atan2} \left(\frac{c(\tau_3) - c(\tau_1)}{c(\tau_0) - c(\tau_2)} \right). \quad (3.14)$$

where atan2 is the 4-quadrant arc tangens.

Fig. 3.4 shows an example for sampling points that would be possible to calculate the phase delay with the 4-Phase algorithm. The phases do not necessarily start a 0 degree shift, but requires equally spaced sampling points of $\frac{T}{2}$. The distance estimation assumes sinusoidal reference in (3.11), therefore the phase estimation in (3.14) is only exact for sinusoidal reference signals. Given a rectangular reference in Fig. 3.4 the estimation will introduce deviation from the real phase, generally known as Circular Distance Error or Wiggling Error (cf. Section 2.2).

Though the 4-Phase algorithm is a common approach, the estimation does not necessarily require 4 phases. Grünwald [15] showed in his thesis the benefits and drawbacks of using only 3 equidistantly spaced phases.

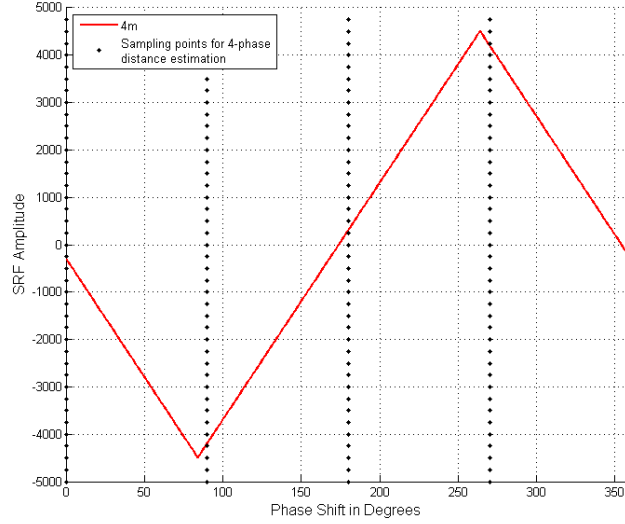


Figure 3.4: Representation of the sampling points used in a 4-phase Algorithm

3.3.2 Fourier method

Another possibility is to derive the distance estimation using the Fourier representation. Starting from the SRF function (3.7) derived in Section 3.2:

$$c(\varphi) = g(d) \cdot \int_0^{\tau} r\left(t - t_d - \frac{\varphi}{2\pi f}\right) \cdot r(t) dt$$

Assume IDFT representation of $r(t)$:

$$r(t) = \sum_{k=-\infty}^{\infty} R[k] \cdot e^{j2\pi k \cdot f \cdot t} \quad (3.15)$$

Insert the spectral representation of the reference signal into the result for the SRF (3.7):

$$\begin{aligned} c(\varphi) &= g(d) \cdot \int_0^{\tau} \sum_{k=-\infty}^{\infty} R[k] \cdot e^{j2\pi k \cdot f \cdot \left(t - t_d - \frac{\varphi}{2\pi f}\right)} \sum_{k'=-\infty}^{\infty} R[k'] \cdot e^{j2\pi k' \cdot f \cdot t} dt \\ &= g(d) \cdot \sum_{k=-\infty}^{\infty} \sum_{k'=-\infty}^{\infty} \int_0^{\tau} R[k] \cdot R[k'] \cdot e^{j2\pi k \cdot f \cdot \left(t - t_d - \frac{\varphi}{2\pi f}\right)} \cdot e^{j2\pi k' \cdot f \cdot t} dt \\ &= g(d) \cdot \sum_{k=-\infty}^{\infty} \sum_{k'=-\infty}^{\infty} R[k] \cdot R[k'] \cdot \int_0^{\tau} e^{j2\pi f \cdot t \cdot (k+k')} dt \cdot e^{-j2\pi k \cdot f \cdot t_d} \cdot e^{-j \cdot k \cdot \varphi} \end{aligned} \quad (3.16)$$

The exponential term under the integral is a multiple of a full period, therefore any value of $k \neq -k' = 0$ in (3.16). This allows the substitution of $k' = -k$ and removes the second summation. Additionally now the integration is performed over and integrand of 1 and the integral can be resolved with its integration period τ .

$$c(\varphi) = g(d) \cdot \tau \cdot \sum_{k=-\infty}^{\infty} R[k] \cdot R[-k] \cdot e^{-j2\pi k \cdot f \cdot t_d} \cdot e^{-jk\varphi}$$

Since the reference signal $r(t)$ is real, the Fourier spectrum is symmetric and it follows that $R[k] = R^*[-k]$.

$$\begin{aligned} c(\varphi) &= g(d) \cdot \tau \cdot \sum_{k=-\infty}^{\infty} |R[k]|^2 \cdot e^{j2\pi k \cdot f \cdot t_d} \cdot e^{jk\varphi} \\ &= \sum_{k=-\infty}^{\infty} \underbrace{g(d) \tau \cdot |R[k]|^2 \cdot e^{j2\pi k \cdot f \cdot t_d}}_{C[k]=A_k \cdot e^{j\varphi_k}} \cdot e^{jk\varphi} \end{aligned} \quad (3.17)$$

Changing the position under the summation then brings (3.17) into a form that is equivalent to the IDFT of the Fourier representation of the SRF $C[k]$ with

$$A_k = \tau \cdot g(d) \cdot |R[k]|^2 \quad \varphi_k = 2\pi k \cdot f \cdot t_d \quad (3.18)$$

(3.17) shows that the Fourier transform of the SRF includes the phase information in the argument of the Fourier coefficients. Assuming again a sinusoidal reference signal the only non-zero Fourier coefficient is $C[1]$ and the target phase can be calculated as:

$$\varphi_d = \arg(C[1]) \quad (3.19)$$

For the complete Fourier transform the result from (3.19) returns the correct distance. If the Fourier transform is only calculated as a N-point DFT for a limited number of points, distance estimation errors will be caused by higher order terms for non-sinusoidal reference signals [15]. For a DFT of length 4 the results is identical to the calculation on the SRF in (3.14) and will result in the same wiggling error for non-sinusoidal signals.

Multipath Propagation in ToF

This chapter introduces the multipath scenario in optical wave propagation. It introduces multipath in general and in particular for ToF imaging in Sections 4.1 and 4.2 respectively. Given a simple multipath channel presented in Section 4.3 the model from Chapter 3 is extended into a multipath signal model in Section 4.4. The impact of MPCs on the sensor response function as well as on the distance estimation is discussed in Section 4.4.2.

4.1 Introduction to Multipath Propagation

Multipath propagation is a typical challenge for all transmission channels. It deals with the different paths that the transmitted signal can take to reach the receiving station. Depending on the exact scene configuration, coherent signals can suffer from destructive or constructive interference depending on the exact phase difference caused by different run times of the MPC. Two major effects are generally considered:

- Small-scale fading - small changes in position cause large changes in interference
- Large-scale fading - caused by objects interrupting the LOS to the receiver (shadowing)

For ToF systems the setup is typically different from RF applications. RF systems often transmit on a channel from transmitter to receiver with either direct LOS or with obstructed LOS introducing shadowing from intermediate objects. ToF systems on the other hand never measure with direct LOS, but always rely on the reflection off an object for its return. Also LOS is not a concern as any object moving in-between the transmitter and its current primary target becomes the new target of interest in most distance measuring applications.

4.2 Sources for Multipath Propagation in ToF Imaging

In current literature, three different types of multipath phenomena are distinguished. From a mathematical point these interferences are identical from the view of a single pixel but each results in unique distortions of the depth image if observed within a real scene. The scenarios of the interference on the image are shown in Fig. 4.1.

The interferences are highly dependent on the scene. For any general observed scene all the given multipath interferences are bound to appear at the same time throughout the image.

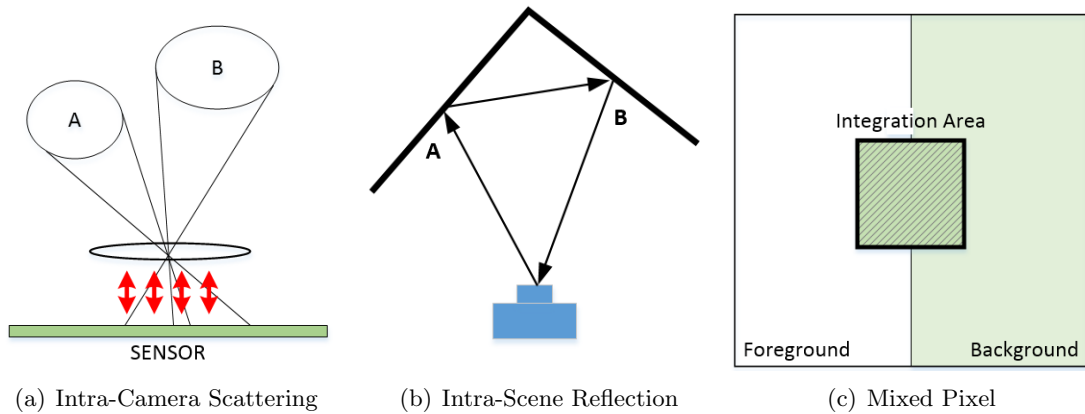


Figure 4.1: Different relevant multipath sources in ToF imaging.

Intra-Camera Scattering

Scattering in RF systems usually deals with scattering on surfaces along the transmission path. For optical imaging systems scattering is an issue on the receiving side due to reflections within the optics of the camera. The incoming light is reflected back and forth between the sensor surface and the lens of the camera optics (Fig. 4.1(a)). This usually happens multiple times spreading the incoming light from one point to all adjacent pixels and creating the typical lens-flare for overexposed regions in images made with optical cameras, as seen in Fig. 4.2.

The scattering effect is a multipath effect that is only loosely dependent on the overall scene configuration. As the effect occurs in the camera optics every pixel generates a typical scattering pattern. Therefore only the location of the scattering pattern is dependent on the scene, not the interference itself.

Scattering onto neighboring pixel does happen for every pixel and is inherent to any optical imaging system. Modern optical lens systems usually have sufficiently good reflective properties to minimize the effect. Only very bright pixels are still able to corrupt neighboring pixels to a sufficient degree to produce measurable errors (e.g. highly reflective surfaces, direct light sources, ...).

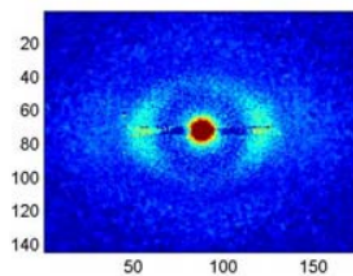


Figure 4.2: Lens flare in an ToF sensor array forced by introducing a highly reflective surface in the center of the array [16]

Within the different multipath sources, scattering has received more interest especially in early research using probability density models to reverse the scattering effect via deconvolution in combination with a statistical model ([1], [17]). Scattering compensation was usually done without further interest in the other multipath sources. These other sources were dismissed as being insignificant compared to the scattering effects.

Intra-Scene Reflections

Intra-scene reflections are the classical multi-bounce reflections described in Section 4.1 that also appear in radar and sonar applications. Research on compensation for reflections within the scene was first done in [18], studying the effect of reflection on a simple corner. A photometric model was introduced in [1] to mathematically model all multiple returns based on the initial measurement of the scene. The model was refined and improved in [2] but still has the disadvantage of being computationally expensive, which is a problem for the model for use in real-time applications. The above approaches focus only on the aspect of multiple reflections and dismiss scattering effects as minimal or at least more being a topic for hardware engineers by using non-reflective surfaces for camera optics to reduce the interference from scattering [13].

Mixed Pixel

Substantially more focus has been put on mixed pixel than on simple intra-scene reflections. The reason for this might be the easy generation of this interference in many experimental setups. Mixed pixel is a phenomenon that appears at sudden depth changes in a scene, as are usually the transition from a foreground object to a background. The effect itself is due to two different depths that are present within the actual integration area of the pixel (Fig. 4.1(c)).

Extensive research on the topic of Mixed Pixel has been done by a research group at Waikato University, NZ [19],[20],[21].

4.3 Modeling Multiple Returns

A standard assumption for the operation of any range imager is the observation of a single return component on each camera pixel. This assumption was also made for the derivation of the AMCW system in Section 3.2, which leads to an impulse response of the optical channel consisting of a single Dirac delta function in (3.3).

As described in Section 4.2, the single return assumption does generally not hold in a realistic scenario. Following the assumption of discrete returns (as was made for the ideal channel response) the channel response of multiple returns can be modeled as the sum of the individual discrete returns from different reflections inside or outside the FOV. This does result in a sparse spike train (SST) model for multiple returns [20]. Two assumptions are made for the channel properties. As we are only interested in observations from a single capture, the scene and therefore the channel is static. We also assume uncorrelated MPCs which allows for a simple superposition of the components.

The impulse of the resulting channel can be described as a simple LTI system with N returns as:

$$h_o(t) = \sum_{i=0}^N h_{o_i}(t) = \sum_{i=0}^N g_i \cdot \delta(t - t_{d_i}) \quad (4.1)$$

where g_i and t_i are the attenuation and time delay of the individual returns respectively. Given that we are generally interested in the closest return component we can write the system as a principal component overlaid by its MPCs.

$$h_o(t) = g_s \cdot \delta(t - t_{d_s}) + \sum_{r=1}^R g_r \cdot \delta(t - t_{d_r}) \quad (4.2)$$

With the principal component being the most direct return in the integration area of the pixel it follows that $g_r < g_0$ and $t_{d_r} > t_{d_0}$ as the additional components need to travel a longer distance

and have additional attenuation due to additional reflections.

4.4 Multipath Signal Model

Using the channel described in the previous section we can now adapt the model for the signal path to incorporate multipath propagation. The change is minor as the only change is in the single transfer function of the propagation channel, as can be seen in Fig. 4.3.

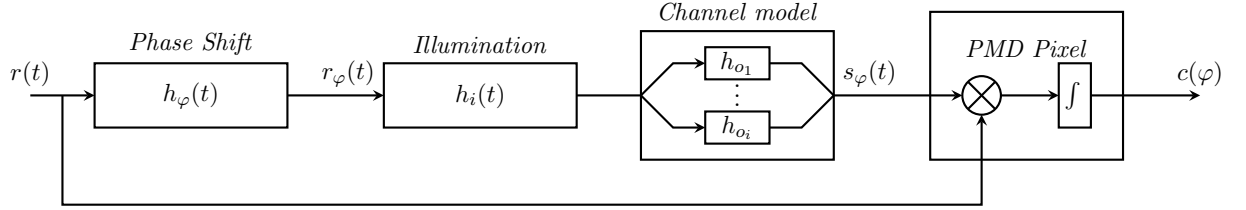


Figure 4.3: Signal model for an AMCW ToF system with multiple returns

4.4.1 Sensor Response Function in MPI

The derivation of the SRF function for the model in Fig. 4.3 is analog to Section 3.2.1.

$$\begin{aligned}
 s_{\varphi}(t) &= h_{\varphi}(t) * h_i(t) * h_o(t) * r(t) \\
 &= \delta\left(t - \frac{\varphi}{2\pi f}\right) * \delta(t) * \left(\sum_{i=0}^N g_i \cdot \delta(t - t_{d_i})\right) * r(t) \\
 &= \delta\left(t - \frac{\varphi}{2\pi f}\right) * \left(\sum_{i=0}^N g_i \cdot r(t - t_{d_i})\right)
 \end{aligned}$$

Using again the properties of the dirac delta function the complete transmission path for the multipath model in (4.1) can be described as:

$$s_{\varphi}(t) = \sum_{i=0}^N g_i \cdot \delta\left(t - t_{d_i} - \frac{\varphi}{2\pi f}\right) \quad (4.3)$$

Processing the correlation in the PMD pixel leads to

$$c(\varphi) = \sum_{i=1}^N g_i \cdot \int_0^{\tau} r(t) \cdot r\left(t - t_{d_i} - \frac{\varphi}{2\pi f}\right) dt \quad (4.4)$$

Therefore the multipath SRF can be shown to be the sum of the SRFs of the individual multipath components with different amplitudes and phase shifts.

4.4.2 Distance estimation in MPI

To determine the influence of the MPI in regards to the distance estimations discussed in Section 3.3 we again switch to a Fourier representation of the SRF.

The derivation is analog to the derivation in Section 3.3.2. Starting again at the IDFT representation of $r(t)$ as

$$r(t) = \sum_{k=-\infty}^{\infty} R[k] \cdot e^{j2\pi k \cdot f \cdot t}$$

we can replace the reference signal in (4.4):

$$c(\varphi) = \sum_{i=0}^N g_i \int_0^{\tau} \sum_{k=-\infty}^{\infty} R[k] \cdot e^{j2\pi k \cdot f \cdot t} \cdot \sum_{k'=-\infty}^{\infty} R[k'] \cdot e^{j2\pi k' \cdot f \cdot (t-t_{d_i} - \frac{\varphi}{2\pi f})} dt$$

Following the same argumentation regarding periodicity of the exponential function and symmetry of the Fourier spectrum we arrive again at a similar result:

$$c(\varphi) = \sum_{k=-\infty}^{\infty} \tau \sum_i g_i |R[k]|^2 e^{j2\pi k \cdot f \cdot t_{d_i}} e^{jk\varphi} \quad (4.5)$$

$$= \sum_{k=-\infty}^{\infty} C[k] e^{jk\varphi} \quad (4.6)$$

Using the distance estimation of the previous chapter we would calculate the argument of the first Fourier coefficient:

$$\varphi_d = \arg(C[1]) \quad \text{with} \quad (4.7)$$

$$C[1] = \tau |R[1]|^2 \sum_i g_i e^{j2\pi \cdot f \cdot t_{d_i}} \quad (4.8)$$

We see that $\arg(C[1])$ will now no longer return the correct phase. Also the 4-phase algorithm can no longer return the correct result even in the case of a sinusoidal reference signal.

4.4.3 Phasor representation of multipath components

The Fourier representation in (4.6) can also be transformed into a phasor representation as the individual components under the sum are already available as amplitude phase components. To simplify the phase model we define a normalized phasor for the fundamental wave in the following form:

$$z = \frac{C[1]}{\tau |R[1]|^2} \quad (4.9)$$

$$= \frac{\tau \sum_i g_i |R[1]|^2 \cdot e^{-j2\pi k \cdot f \cdot t_{d_i}}}{\tau |R[1]|^2} = \sum_i g_i \cdot e^{-j2\pi k \cdot f \cdot t_{d_i}} \quad (4.10)$$

$$= \sum_i z_i \quad (4.11)$$

We can again split the signal into a principal component with the target distance and the additional MPCs.

$$z = z_s + \sum_r z_r$$

with:

$$z_s = g_s \cdot e^{-j2\pi \cdot f \cdot t_d} \quad z_r = g_r \cdot e^{-2\pi \cdot f \cdot t_{dr}} \quad (4.12)$$

Fig. 4.4 shows a multipath return scenario in the phasor model for two components, one primary component z_s and one multipath component z_r . In real-world scenarios more than two components may be present which add additional phasors. Given the relation in (4.8) the resulting phase using the simple approach of Chapter 3 can be calculated as

$$\varphi_d = \arg(z)$$

which again includes the errors introduced by the additional components z_r . The error caused by the additional components is relative to the amplitude and phase of the sum of the components. E.g. the phase errors caused by the same MPC z_r is higher for a smaller primary component (Fig. 4.4 right)

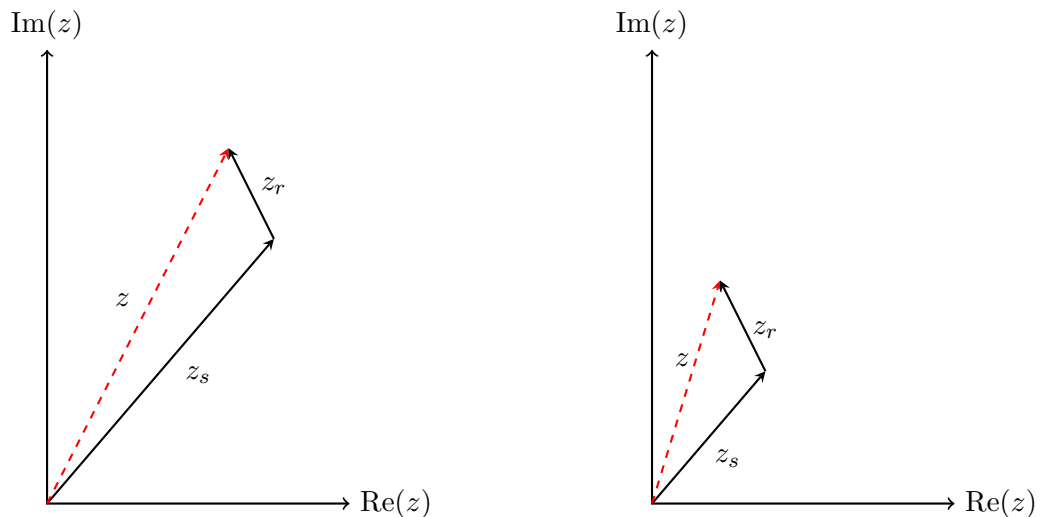


Figure 4.4: Phasor interpretation for two component return with different primary component amplitudes

The error caused by the multipath component z_r is shown in Fig. 4.5. For a fixed phase error an increase in relative amplitude of the disturbing return causes also an increase in multipath error. If the relative amplitude is fixed, the changing phase difference to the principal component causes an error that is periodic in distance.

The resulting phasor in Fig. 4.5 shows the maximum phase error possible for the given amplitude of z_r . Depending on the actual phase of the MPC the interference can be constructive or destructive in distance.

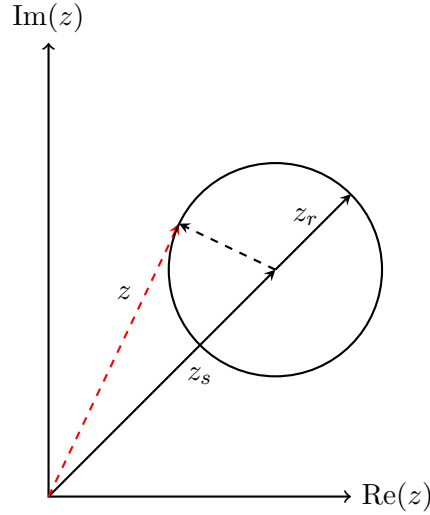


Figure 4.5: Phase error caused by a single multipath component and its influence on the phase error given a variable MPC phase.

Ambiguity of the SRF with MPI

The single path SRF is defined as:

$$c(\varphi) = \int_0^{\tau} g(d) \cdot r\left(t - t_d - \frac{\varphi}{2\pi f}\right) \cdot r(t) dt$$

As shown in (4.4) the SRF for the multipath case is the sum of the individual SRFs.

$$\begin{aligned} c_{mp}(\varphi) &= \int_0^{\tau} \sum_{i=1}^R g_i(d) \cdot r\left(t - t_{d_i} - \frac{\varphi}{2\pi f}\right) \cdot r(t) dt \\ &= \sum_{i=1}^R \int_0^{\tau} g_i(d) \cdot r\left(t - t_{d_i} - \frac{\varphi}{2\pi f}\right) \cdot r(t) dt \\ &= \sum_{i=1}^R c_i(\varphi) \end{aligned}$$

The resulting SRF shape is depending on the original reference and return signal. Given a perfect rectangular reference signal and perfect illumination as used in Fig. 3.3 the resulting SRF is shown in Fig. 4.6. The resulting SRF shows discontinuities at the positions of the maxima of the individual SRFs.

An exact enough sampling of the SRF in Fig. 4.6 would allow to resolve the individual components. The maximum is still recoverable as well as the other multipath component. This is generally not achievable as the illumination signal usually will not be rectangular due to low-pass behavior of the illumination circuits². Depending on the modulation frequency of the reference signal and the cut-off frequency of the illumination the signal shape will be close to sinusoidal.

For sinusoidal reference signals the superposition of SRFs again leads to a sinusoidal SRF. Even

² The reference signal on the direct path to the pixel will also deteriorate in practice even if an ideal rectangular signal can be generated.

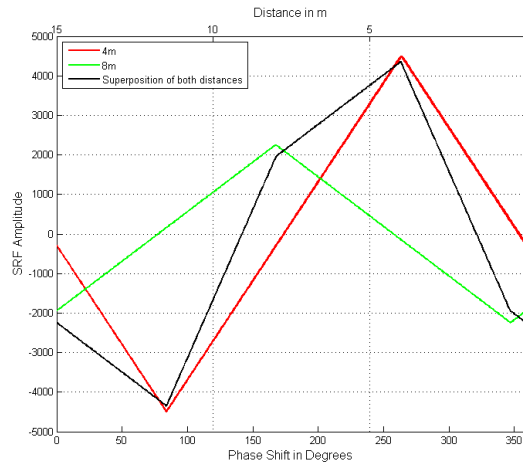


Figure 4.6: Multipath SRF and individual SRFs for ideal rectangular reference signal at $f_{mod} = 10\text{MHz}$

with an infinitesimal sampling of the SRF it is not possible to find the two or more different components in Fig. 4.7.

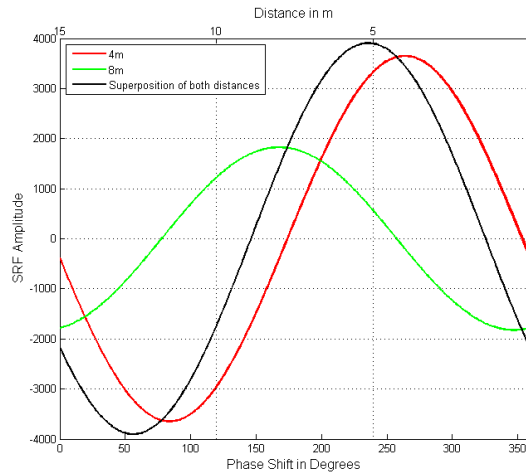


Figure 4.7: Multipath SRF and individual SRFs for sinusoidal reference signal at $f_{mod} = 10\text{MHz}$

Multipath Interference Compensation

This chapter introduces several possibilities to identify individual MPCs with the goal of limiting the distance error caused by them. Section 5.1.1 introduces the multipath interference compensation problem as a common channel estimation problem comparable to channel sounding methods and shows the general inadequacy of the AMCW approach for classic channel estimation. Several compensation frameworks are then discussed in Sections 5.2 to 5.4 to address the shortcomings of the AMCW ToF System.

5.1 Introduction to MPI

As shown in Section 4.4.1, periodic illumination waveforms are not suitable to identify multiple component returns without at least considerable effort spent in exact sampling of the SRF. As the illumination signal deteriorates into a sinusoidal shape, high sampling of the SRF might also be insufficient. Therefore it is necessary to explore different approaches to gain enough information about the multipath effects from the sensor data to distinguish individual components.

5.1.1 MPI as channel estimation problem

Another way to look at the identification of the signal path presented in Fig. 4.3 is in the form of a channel estimation for the optical path $h_o(t)$. With the correlation of the PMD pixel, the signal flow is equivalent to the general principle of a correlative channel sounder.

For a channel sounder the TX sends a defined signal and the RX stores the result to calculate the time-variant or time-invariant impulse response of the channel. The PMD pixel inherently implements the correlation step between RX and TX.

The following are properties of the sounding signal that are important for efficient measurement of the impulse response in a channel sounder [22]:

- **Large Bandwidth:** The bandwidth determines the achievable delay resolution, with higher bandwidth allowing finer resolution
- **Time-Bandwidth Product:** A high TW product allows the transmission of high energy in the sounding signal, obtaining a higher SNR
- **Signal duration:** Longer signal duration are obviously beneficial for a high Time-Bandwidth Product, but need to be low enough to be able to view the channel as stationary during measurement
- **Power Spectral Density:** A uniform PSD across the bandwidth of interest allows for equal accuracy across all frequency components
- **Correlation Property:** Specifically for correlative sounding an ACF with high Peak-to-off-Peak ratio and zero mean is required

Given the reference signal, we assumed for AMCW ToF the properties are not met for the most part:

- The bandwidth is severely limited by the illumination circuit
- Signal duration can be chosen quite long to achieve a reasonable SNR as we assume a time-invariant channel
- The PSD is basically only a single frequency for a sinusoid and still very non-uniform even if rectangular signals could be assumed
- With the simple periodic reference signal the ACF is also periodic

The reference signal used for AMCW ToF is therefore completely inadequate to resolve the impulse response of the channel. To allow the estimation of the impulse response the reference signal needs to be adapted.

For a time-domain approach the ACF of the signal needs to be changed to more favoring properties. This could be done by changing the reference signal completely and replace the simple periodic signal by a coded or swept reference signal with an more ideal ACF. The use of maximum-length sequences for coded modulation was shown in [5].

A frequency-domain approach usually employs frequency-sweeping reference signals like chirps to generate a uniform PSD.

Following are the approaches that are discussed in current literature.

- Intra-Scene Reflection Modeling
- Multifrequency Methods
- Correlation Waveform Deconvolution

5.2 Intra-Scene Reflection Modeling

If the scene is known, multipath propagation paths can be calculated and compensated analytically. This was first shown by Fuchs [1] using the assumption of Lambertian radiators for the scene objects and also includes a scattering model for the sensor [17]. This approach requires detailed knowledge of the scene and has considerable computational complexity depending on the scene configuration.

For this thesis, this method is not investigated further as the scope is not on known scene configurations but is looking for multipath interference compensation in general settings.

5.3 Multifrequency Compensation

AMCW ToF sensors usually do not allow sweeping frequency signals. But it is usually possible to specify the modulation frequency used either continuously with certain resolution or at few specified frequencies. This essentially allows to build the sweeping input signal by measuring the distance at multiple frequencies. From the distance calculation in (2.1) we can easily derive the effect of different modulation frequencies on the phase return. The phase difference due to the traveled distance of the modulated light is given by:

$$\varphi = d \cdot \frac{4\pi}{c} \cdot f_{mod} \quad (5.1)$$

Given an arbitrarily different frequency $f'_{mod} = k \cdot f_{mod}$ with the multiplicative factor $k \in \mathbb{R}$ we use (5.1) to derive the relation of φ to f_{mod} assuming a constant target distance d .

$$\begin{aligned}
\varphi' &= d \cdot \frac{4\pi}{c} \cdot f'_{mod} \\
&= d \cdot \frac{4\pi}{c} \cdot k \cdot f_{mod} \\
&= k \cdot d \cdot \frac{4\pi}{c} \cdot f_{mod} = k \cdot \varphi
\end{aligned}$$

This presents us with the straightforward relation:

$$k \cdot f_{mod} \Rightarrow k \cdot \varphi \quad (5.2)$$

This is also intuitively explained as higher frequencies have smaller periods while the distance t_d - and with it the time delay of the return - stays constant. The relation in (5.2) is theoretically correct, but in practice the phase difference φ is only defined within $[0, 2\pi)$ as the phase error is the result of a correlation measurement. Therefore we have to deal with phase wrapping, because any $\varphi > 2\pi$ is wrapped into the interval $[0, 2\pi)$.

Using the result in (4.11) we can build a model for multifrequency compensation.

$$z(k) = \hat{g} \cdot e^{j\hat{\varphi}(k)} = g_s \cdot e^{jk\varphi_s} + \sum_{r=0}^R g_r \cdot e^{jk\varphi_r} \quad (5.3)$$

The phases of each component change proportional to the change in modulation frequency. Unfortunately this is not the case for the overall phase of the measured signal, since the relation is non-linear.

5.3.1 Nonlinear Regression

As a straightforward solution to the problem in (5.3) we can look at a non-linear optimization method that solves this equation. Dorrington et. al. [19] used a least squares approach but limited the model to only two possible multipath components. To use a similar approach it is possible to use non-linear least squares analysis for arbitrarily many multipath components. Specifically applicable for (5.3) is the separable non-linear least squares (SNLLS) method, which has as an underlying model a linear combination of non-linear functions. The residual can be written as:

$$r(\mathbf{g}, \varphi) = z(k) - \sum_i g_i \Phi_i(\varphi, k) \quad (5.4)$$

The attenuation vector \mathbf{g} and the phases φ for the individual components are the parameters to be determined, with Φ_i as the non-linear function.

The matrix form for the least-squares solution of (5.4) can be written as:

$$\|r(\mathbf{g}, \varphi)\|_2^2 = \|z - \Phi(\varphi)\mathbf{g}\|_2^2 \quad (5.5)$$

The algorithm then works by iteratively optimizing for the non-linear parameters φ and then solving the linear least squares problem for g_i under a constant non-linear term [23].

Closed-Form Inverse

For the special case of only two return components, a closed form inverse solution exists [3]. The inverse requires measurements at exactly four equidistant modulation frequencies and also takes into account reflectivity of the surfaces. The method requires sufficient SNR and relative amplitude of the MPC to improve on the uncorrected phase error. Due to the non-linear nature of (5.3), no closed-form solution has been found for MPI with more than two return components. The case of multiple returns requires numeric optimization algorithms.

5.3.2 Spectral Estimation

The spectral estimation problem can be stated on the sum of p complex exponentials in the presence of white noise $w(n)$ [24]:

$$x(n) = \sum_{i=0}^{p-1} a_i \cdot e^{jn\varphi_i} + w(n) \quad (5.6)$$

The equation in (5.6) is equivalent to the result of the multifrequency result in (5.3) under influence of white noise.

Having identified the multifrequency approach as a spectral analysis problem, it is possible to estimate the unknown parameters a_i, φ_i using well-researched methods from the field of spectral estimation. Looking at the literature some approaches to solving the multifrequency problem do use a spectral estimation technique without specifically defining it as a spectral analysis problem [19].

5.3.3 Linear Regression

The already mentioned possible solutions to the multifrequency problem are computationally expensive. MUSIC requires among other things the calculation of Eigenvalues and the non-linear regression requires iterative approximation. If the MPI compensation needs to be calculated for each image, this might not be possible at higher frame rates. For two multipath components a closed-form inverse exists that is fast to compute, but is also very restrictive in the number and choice of frequencies [3].

A different, simple approach is the use of linear regression. Given the phasor model of Chapter 4:

$$z(k) = \sum_{n=0}^N a_n \cdot e^{jk\varphi_n}$$

If no multipath return were present the resulting phase delay would simply be linear over frequency with

$$\varphi_k = k \cdot \varphi_d$$

As shown in Chapter 4 multiple returns can be represented as phasors rotating on top of the principal component. Different frequencies cause the individual components to rotate at different speeds. This causes a periodic phase error relative to the principal phase delay (Fig. 5.1).

Assuming that the chosen frequencies cover a complete period of the periodic phase error the MPI could be removed completely. Compared to the spectral estimation and non-linear regression methods the linear regression has the following advantages:

- Low computational complexity

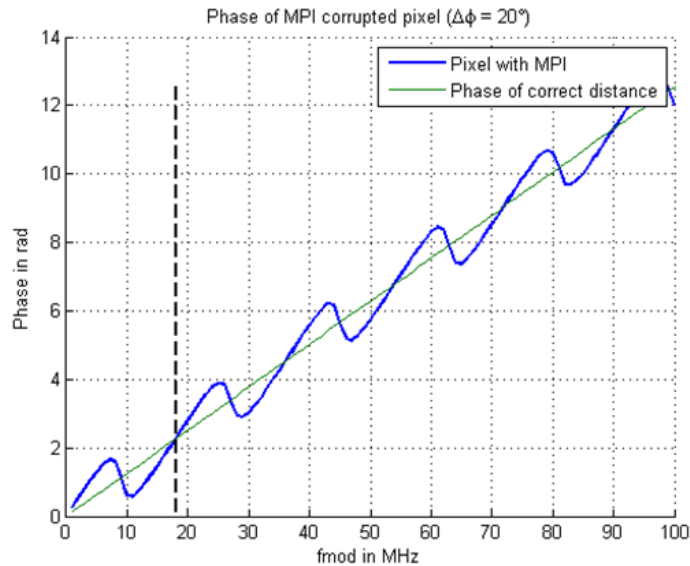


Figure 5.1: Phase return simulated over frequency for a two component return.

- No equidistant frequency sampling required
- No prior knowledge of the number of components required

The method has some shortcomings though:

- Higher residual error if not evaluated over complete periods
- No information on the other MPCs recoverable
- Absolute phase delay required (phase unwrapping)

Phase unwrapping

As mentioned in the disadvantages of the method, the linear regression requires the absolute phase delay over the complete frequency range. This means that phase unwrapping has to be done before the MPI compensation can be performed. Fig. 5.2 shows the measured phase delay with two return components and its recovered absolute phase. The measured result is restricted to the interval $[-\pi, \pi)$.

5.4 Correlation Waveform Deconvolution

The use of periodic sinusoidal signals is very problematic for resolving multiple return components as shown in Section 5.1.1. One solution is to move away from the AMCW reference signal and use signal forms that more adequately fulfill the requirements for efficient channel estimation. One possibility was shown by Kadambi et.al. [5], using coded modulation instead of AMCW signals. It avoids the ambiguity problem in the SRF by using broadband or pseudo-random codes (e.g. m -sequences) to generate reference signals with broadband spectra and suitable ACF.

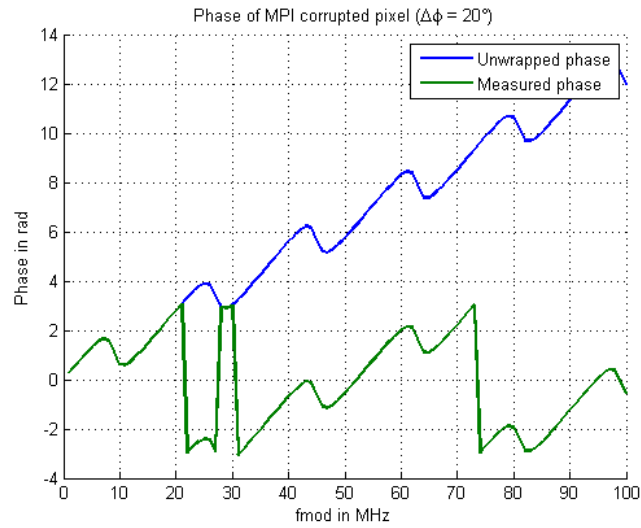


Figure 5.2: Measured and unwrapped phase of two component return.

State-of-the-art ToF cameras usually do not have the option to generate illumination signal based on random codes and have to be heavily modified (as was done in [5]) to produce those signals. Also the camera used in Chapter 6 is not capable of signals other than rectangular waves, therefore this option cannot be investigated in practice.

Simulations and Experiments

This chapter presents simulation results of the model presented in previous chapters and an experimental setup using a commercially available 3D-Imaging camera.

6.1 Simulation Framework

As was mentioned numerous times in the previous chapters, multipath phenomena are dependent on the scene configuration. To explore the properties and magnitude of multipath related errors reliably, simulations are an easy alternative to gain insight. Simulations allow to:

- change individual parameters of a single pixel return without affecting the other properties
- add or remove error sources on the pixel

The simulation is modeled according to the signal flow graph in Fig. 3.2. The implementation is done in MATHWORKS[®] MATLAB[®] in Version 2014b. The model offers the following possible properties:

- Simulation of an arbitrary number of multipath returns on a single pixel (that is otherwise hard to reliably produce in real-world scenery)
- Variable return length and return intensity (independent of each other)
- arbitrary number of phase shifts
- adjustable SNR
- optional low pass filter for illumination
- arbitrary illumination signal (both for signal form and frequency)

As pointed out the simulation only focuses on a single independent pixel. Influences of neighboring pixels (e.g. in the case of scattering) are not taken into account explicitly, but can be modeled as additional return signal on the pixel.

The simulation also allows for a statistical evaluation of the compensation algorithms presented in Chapter 5.

6.2 Measurement Setup

6.2.1 Setup Overview

The measurement setup is quite simple as can be seen in Fig. 6.2. The two main components are:

- State-of-the-art ToF imager (Tab. 6.1)



Figure 6.1: Imager setup. Sensor is central on the board with optics. The LED illumination is positioned above the sensor.

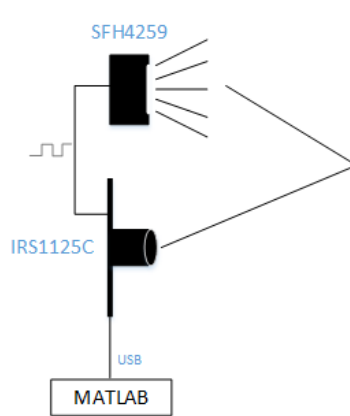


Figure 6.2: Block diagram of the measurement setup.

- An illumination unit (8x8 OSRAM SFH4259 LED-block)
- A PC with MATHWORKS[®] MATLAB[®]

The illumination unit is external but directly controlled by the ToF imager, using a rectangular waveform with an adjustable frequency. Frequency, phase shifts and most other properties of the imager are set directly from within the MATLAB capture sequence using a USB connection to the imager via a provided library. The capture sequence of the imager is initiated via MATLAB and returns all phase images as a single MATLAB matrix for post-processing.

Manufacturer	Infineon Technologies AG
Type	IRS1125C
Resolution	352 x 288
Modulation Frequency	3MHz - 100MHz
Frequency Resolution	$< 1kHz$
Optical Wavelength	850nm

Table 6.1: Specification of the used ToF Sensor

6.2.2 Calibration

Usually, for any application, extensive calibration has to be performed to acquire precise distance measurements [6]. For the purpose of the measurements pertaining to multipath propagation, not all calibrations are relevant. Only calibrations are done that could influence the result of the experiments regarding multipath interference.

Illumination signal delay

Frequency depending phase delay

ToF camera calibration is generally only necessary for the application frequencies. With multi-frequency measurements also additional effort needs to be spent in removing possible distance deviation caused by different modulation frequencies.

Distance errors could be caused by:

- Changing illumination signal shape (low-pass of the illumination)
- Changing illumination duty cycle (caused by the illumination driver)
- Changing reference signal shape or duty cycle on chip

Fig. 6.3(a) shows the absolute distance measured on three static distances to a flat surface for the complete frequency range. Given the real distance of the surface the distance error (Fig. 6.3(b)) can be calculated as:

$$e_i(f) = d_i(f) - \hat{d}_i$$

with d_i as the measured distance and \hat{d}_i as the real target distance for each calibration distance.

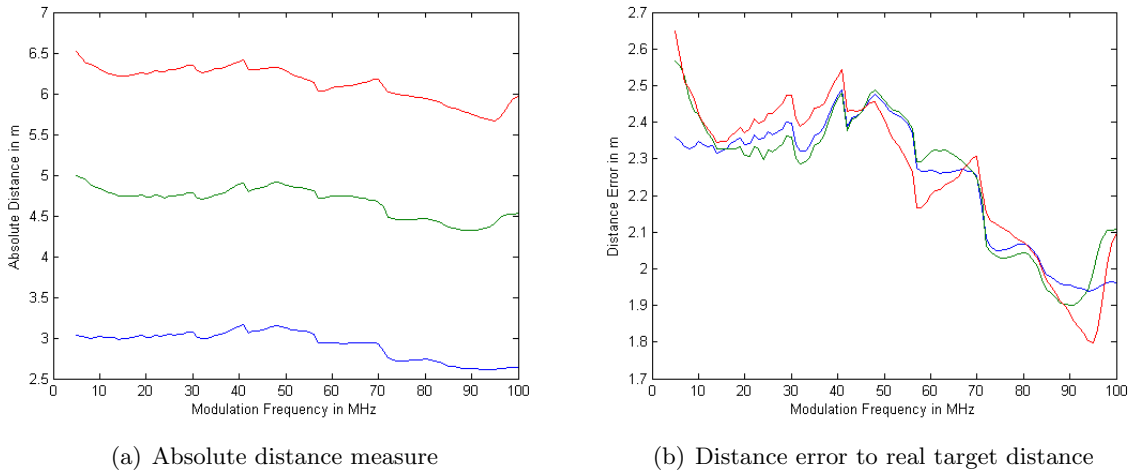


Figure 6.3: Distance measurement for the imager frequency range

The calibration values used are then calculated as the mean of the distance error for all distances.

$$e(f) = \text{Avg}\{e_i(f)\}$$

The difference in error between the three distances is quite similar. If there would be a significant difference between multiple distances then the calibration might be required to also distinguish target distance instead of averaging into a single calibration vector. As the calibration uses the real target distances, the corrected value will also do a simple global offset correction on the image.

Optical distortions

Radial Distance Error

A flat surface will not be measured flat due to different distance based on the sensor being a

point source directed in a specific FOV. The surface at the edge of the FOV will be naturally further away than central areas (Fig. 6.4).

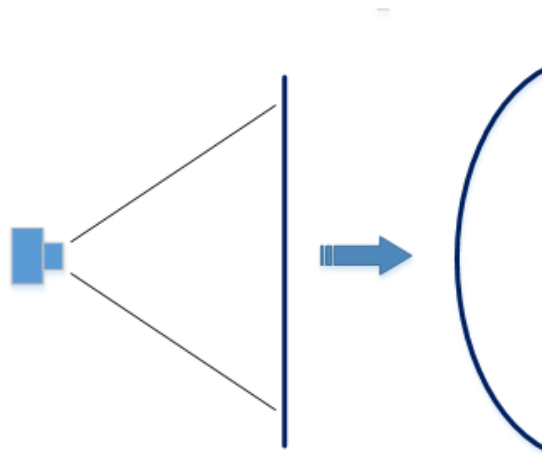


Figure 6.4: Radial distance error caused by optical setup.

The radial distance error is not calibrated, as all measurements are interested in relative changes in distance. An absolute error is not relevant to the experiments done.

Illumination position

An external LED block is used for scene illumination. The non-centric position of the illumination unit relative to the sensor (Fig. 6.1) causes an error in the depth measurements. Ideally illumination is at the same position as the sensor to avoid different path length on different sides of the imaging plane. As illustrated in Fig. 6.2 the position of the light source does have a deterministic effect on the path length (and therefore on the depth measurement) of the scene. Again, the non-centric position of the illumination only affects the absolute distance along the scene and is not a problem for relative distance measurements.

Fixed Pattern Phase Noise

Fixed Pattern Phase Noise is an effect caused by differences between the pixels and the readout circuits. This effect caused small differences in distance between pixels. This distance error is generally constant as causes are usually found in the layout of the sensor and deviations in the production process. As with general distance offsets, this is not concerning for the experiments as only relative changes in difference are relevant.

6.2.3 Measurement Scenarios

With the availability of a ToF imager the simulated results can be checked against captured data. Due to the scene-dependent nature of multipath propagation and the complex calibration of camera systems, the measurements are only used to qualitatively verify or dismiss the theoretical and simulated results.

The questions that this thesis wants to answer are:

- How big is the influence, if any, due to multiple returns on a ToF pixel?
- Is it practically possible to achieve reasonable compensation of multipath related errors using the ToF imager setup in Section 6.2=

- What are the limitations and possible improvements to increase the performance of MPI algorithms?

To answer these questions, appropriate scenes are constructed and captured to show the effect on the depth information of the scene. The scenes are kept simple (mostly single objects) to focus on a single effect, rather than combining them in more complex setups. Compensation algorithms can then be tested on the erroneous depth images to evaluate their quality.

6.3 Simulation of Multiple Returns

The effect of multipath can be studied at a single pixel alone. Though some effects are contributing to the return on a pixel (e.g. scattering from neighboring pixel) the mathematical description is independent from the source of the returning light. Therefore it is still useful to look at the influence of multiple return signals for a single pixel.

6.3.1 Single Multipath Return

In most available literature the case of multiple returns is reduced to the special case of a single return. This allows for a deterministic evaluation of the multipath error, due to the limited number of parameters that influence the depth measurement.

The parametrization is based on the phasor interpretation where the resulting phasor is defined as:

$$z = z_s + z_r$$

The phase error can be calculated relative to the principal phasor z_s as:

$$e_\varphi = \arg\left(\frac{z}{z_s}\right) \quad (6.1)$$

with (4.12):

$$\left(\frac{z}{z_s}\right) = 1 + \frac{g_r \cdot e^{j2\pi \cdot \varphi_r}}{g_s \cdot e^{j2\pi \varphi_s}} \quad (6.2)$$

$$= 1 + \frac{g_r}{g_s} \cdot e^{j2\pi(\varphi_r - \varphi_s)} \quad (6.3)$$

$$= 1 + a_r \cdot e^{j2\pi \Delta\varphi} \quad (6.4)$$

$$(6.5)$$

The simulation vary both amplitude and phase of the multipath phasor independently and relative to the principal component to see the effect on the phase error based on the two parameters. Fig. 6.5 shows the effect of the variation in terms of the phasors.

For an increasing relative amplitude a_r the phase error increases as well. The sign of the phase error caused by amplitude variation will not change. In Fig. 6.6 only phase differences³ $\Delta\varphi < 180$ are plotted, so only multipath phasors in the upper half circle of Fig. 6.5(a) are used. Phasors in the lower half circle would generate a negative phase error.

Varying the phase difference of the MPC the resulting phasor has a periodic phase error (Fig. 6.7(a)). The maximum phase error changes in position and amplitude depending on the

³ The symbol φ is not available in Matlab, ϕ is used instead.

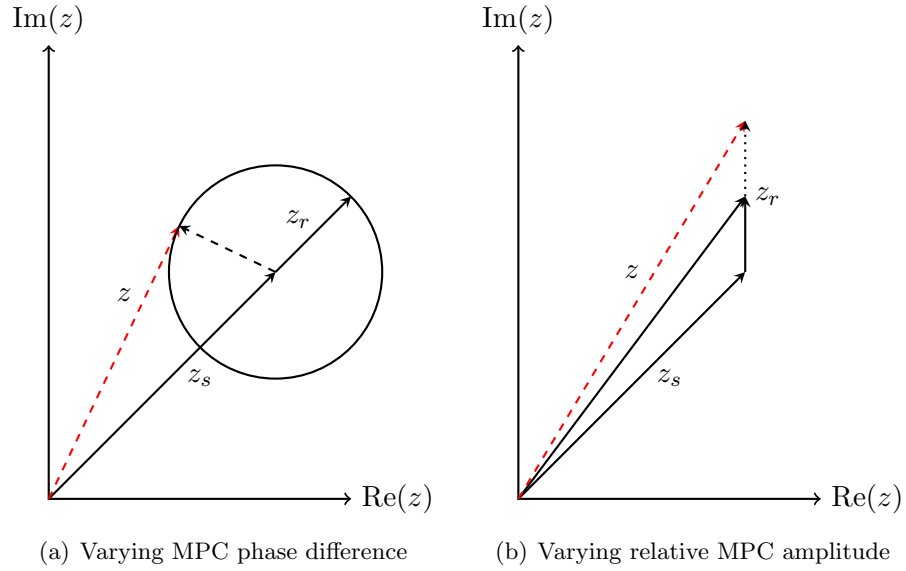


Figure 6.5: Effect on phase error for a single MPC with varying phase or amplitude.

relative amplitude of the MPC. The maximum phase error $e_{\varphi,max}$ and its phase difference $\Delta\varphi_{max}$ can be simply calculated as the maximum error is at the tangential point of the circular error.

$$e_{\varphi,max} = a \sin(a_r) \quad (6.6)$$

$$\Delta\varphi_{max} = a \cos(a_r) \quad (6.7)$$

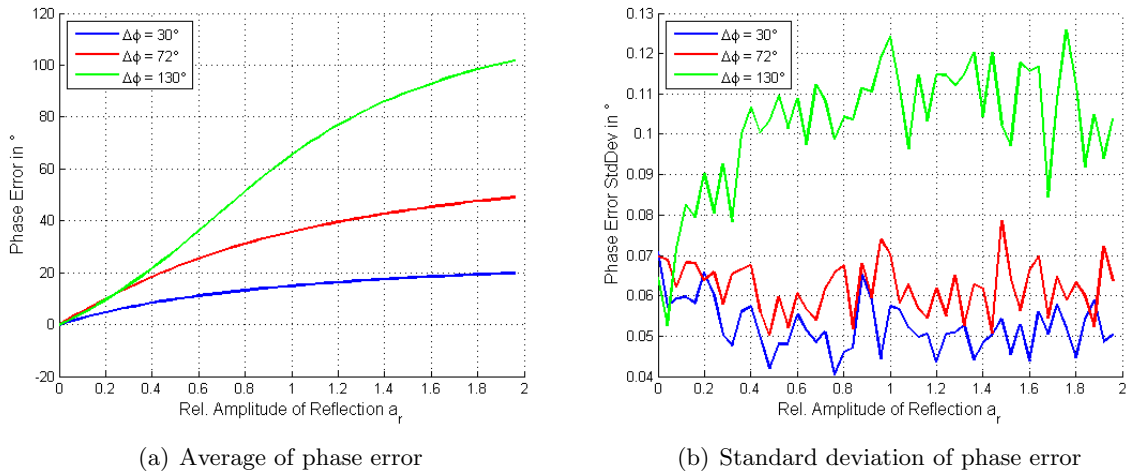


Figure 6.6: Phase error and standard deviation for a single multipath return and variable relative amplitude of the multipath component for a sample size of $N = 100$.

Wiggling Error in MPI

The maximum phase error possible by a single MPC in (6.7) only holds for sinusoidal reference signals. We know from general calibration that the circular distance error (wiggling) is dependent on the target distance. With changing $\Delta\varphi$ and a_r the distance of the resulting phasor z effectively

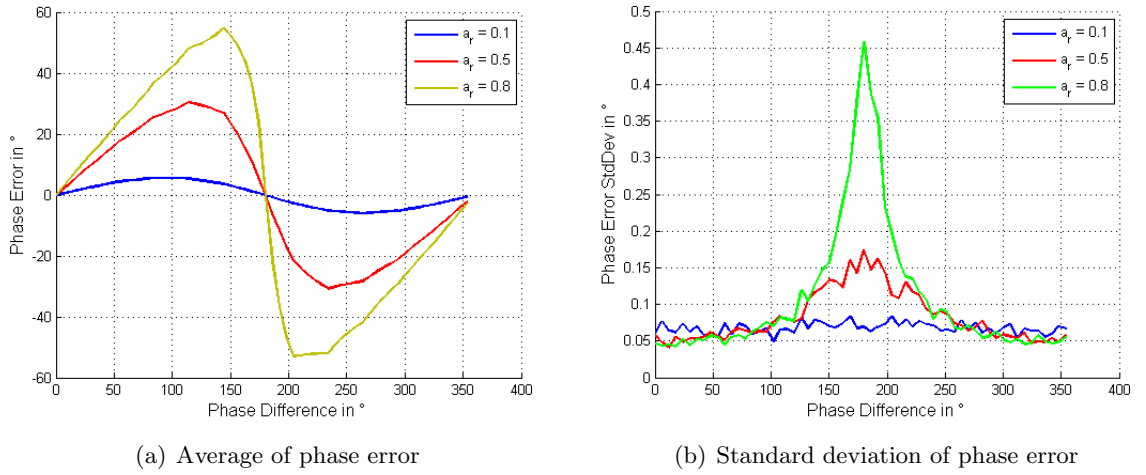


Figure 6.7: Phase error and standard deviation for a single multipath return and variable relative phase difference of the multipath component for a sample size of $N = 100$.

changes and therefore wiggling can also be seen in Fig. 6.8.

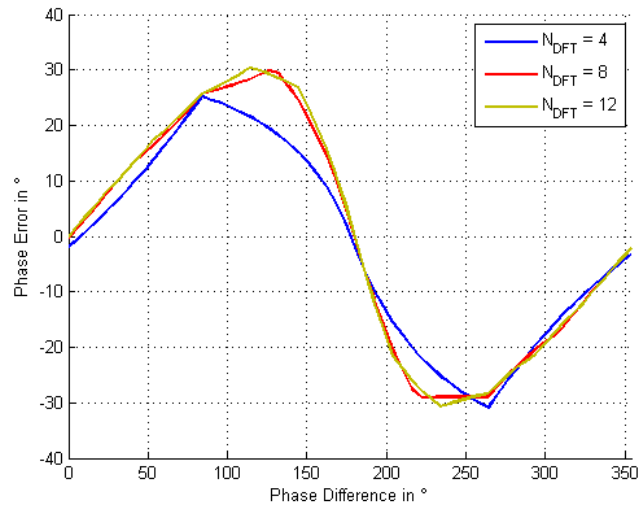


Figure 6.8: Phase Error for different DFT lengths for $\Delta\varphi = 0.5$ and $a_r = 0.5$.

Fig. 6.8 shows the effect of the wiggling error for different DFT lengths that are used to calculate the distance from the resulting SRF:

$$\phi_z = \arg(C[1])$$

$$C[k] = \frac{1}{NDFT} \sum_{n=0}^{NDFT-1} NDFT - 1c(\varphi) \cdot e^{-j2\pi \frac{k \cdot \varphi_n}{NDFT}}$$

The values φ_n are equidistantly spread on the SRF. With $NDFT = 4$ we get the 4-phase algorithm shown in Section 3.3. Increasing the length of the DFT reduces the influence of the wiggling error.

Therefore even if wiggling might not generally be a problem (as results are required only relative to each other and wiggling is constant for a single target distance) it needs to be considered for

changing multipath components.

Including additional MPCs

Additionally to the scenario of a single multipath only we also want to quickly look at the effect of additional MPCs to the phase error as shown in Section 6.3.1. This is done with two special cases.

The case shown in Fig. 6.9(a) is a second multipath component normal and anti-normal to the direction of the principal component with the same amplitude as the other component. This causes an offset of the phase error proportional to the amplitude difference of the components. In Fig. 6.9(b) the second multipath component is in the same and opposite direction of the principal component respectively. Even though a single multipath component in the same or opposite direction of the principal phasor does not cause phase error, in combination with another multipath component this does indeed change the resulting phase error. Basically, it increases or decreases the relative amplitude a_r of the non-parallel MPC.

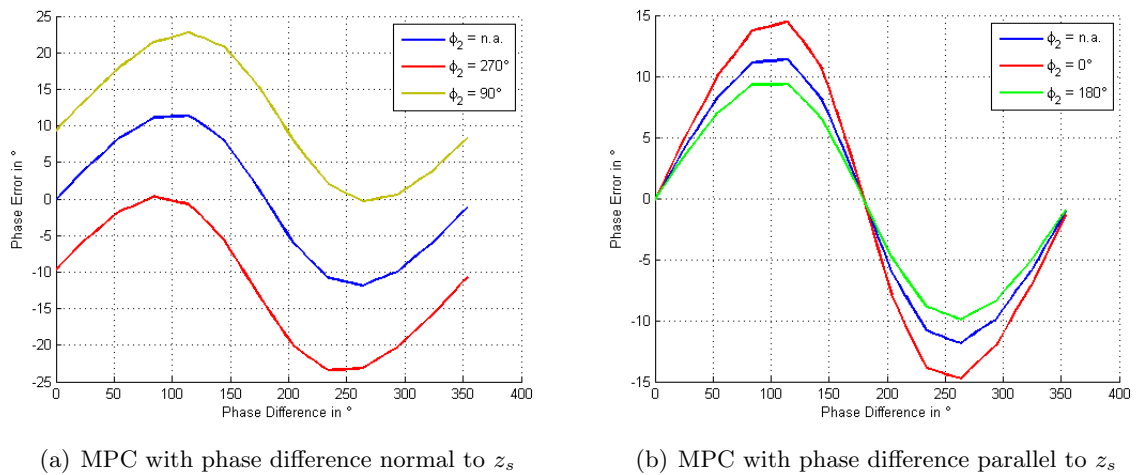


Figure 6.9: Phase Error with two MPCs. The second MPC is in different static phase configurations.

The data in Fig. 6.9 shows that the phase error, though quite simple for a single MPC, can get very complex for an increasing number of components. The resulting phase error can be increased greatly or also reduced given the correct combination of multipath components.

6.3.2 Multifrequency Return

The same calculations as in the previous section can be done with varying frequency instead of phase. Due to the relation shown in (5.2), frequency and phase are interchangeable. For the phasor model this means that the MPCs will rotate with different speeds depending on the distance of the individual components, while the undisturbed phase would be a simple linear relation. Relative to the principal components the MPCs therefore show a different phase difference for every frequency. This means that the periodic phase error shown for a changing MPC phase in Fig. 6.7(a) will be present for varying frequency as well. This periodic error can be seen in the phase result in Fig. 6.10.

The period of each interference in Fig. 6.10 can be calculated as:

$$T_f = \frac{c}{2 \cdot \Delta d} \quad (6.8)$$

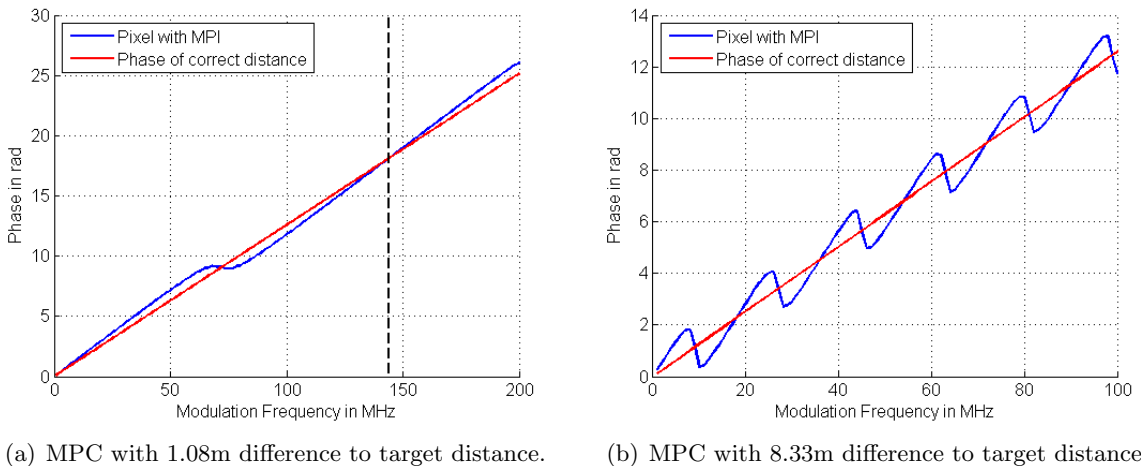


Figure 6.10: Phase over modulation frequency of resulting phasor for a target at 3m with a single MPC at different lengths.

where c is the speed of light and Δd is the length difference of the MPC to the principal component.

Fig. 6.11 shows the phase for two multipath components as a function of f_{mod} . The MPCs add on top of the correct distance phase and again generate a periodic disturbance. The period of the disturbance is neither 18MHz or 30MHz for 8.33m and 5m respectively, but the largest common multiple for both periods, in this case 90MHz.

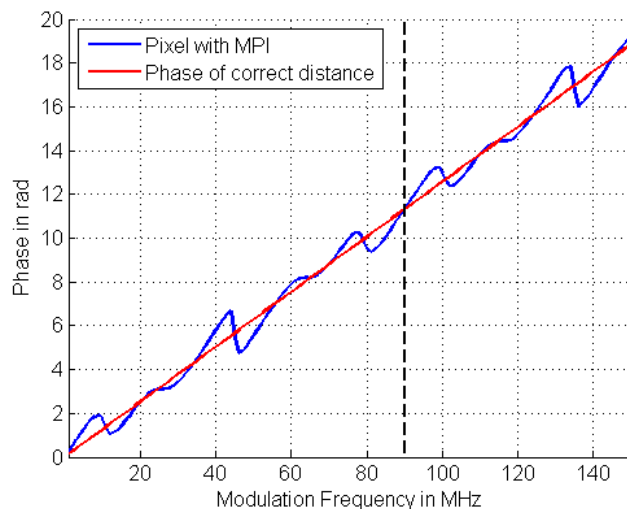


Figure 6.11: Phase over modulation frequency of resulting phasor for a target at 3m with two MPC with 5m and 8.33m distance difference.

6.3.3 Simulated MPI Compensation

Given the results of the model in Section 6.3.2 we can use the phase error for different frequencies to compensate the multipath error using different algorithms for multifrequency MPI compensation. The following algorithms are used:

- Separable non-linear least squares (SNLLS)

- MUSIC
- Linear Approximation

The following parameters can be varied:

- Multipath components
- Max. modulation frequency
- Number of frequency points
- DFT length in phase calculation
- SNR of signal returns

As MUSIC only works for equidistant frequency points, all simulations will be done within this constraint, although the other methods are free in the choice of frequencies.

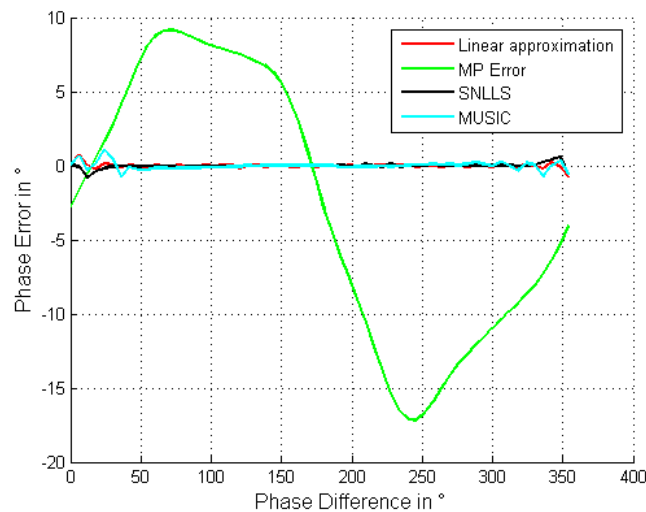


Figure 6.12: Phase Error for MPIC Algorithms - 1 MPC, NDFT = 4, $f_{mod} = 10:10:100\text{MHz}$, SNR = 10dB

Fig. 6.12 shows the residual phase error for the algorithms for a single MPC over the full range of phase difference. All algorithms looked at in this section show significant phase errors only for small phase differences of the multipath component. Therefore all other observation will also focus on small phase differences only.

The residual error for different DFT lengths in the phase estimation is shown in Fig. 6.13. All three algorithms are not able to remove the multipath interference for small phase differences. But the multipath is reduced quite well for any phase difference $> 10^\circ$ for SNLLS and MUSIC for a DFT length of 12. The higher residual for NDFT = 4 is caused by the error in the phase estimation. As mentioned in Section 4.4.2, the distance estimation is only correct for sinusoidal modulation signals (the simulation uses a low-pass filtered rectangular reference signal). The estimation algorithms can only deal effectively with white noise. The non-white noise generated from the incorrect phase estimate causes the residual error for low DFT lengths.

The error of the linear approximation is mostly independent of the DFT length. As explained in Section 5.3.3 this approach only compensates perfectly if the error is compensated over full periods in the phase error. This is the case at the zero-crossings in the residual error.

The returns used in Fig. 6.13 are calculated with relatively high SNR of 30dB. The result for an SNR of 10dB is shown in Fig. 6.14. The noise is generated as additive white Gaussian noise and has no impact on the residual error of the algorithms. SNLLS and MUSIC are insensitive to AWGN by design and the linear approximation is basically an average, where white noise will not disturb as long as it is zero-mean.

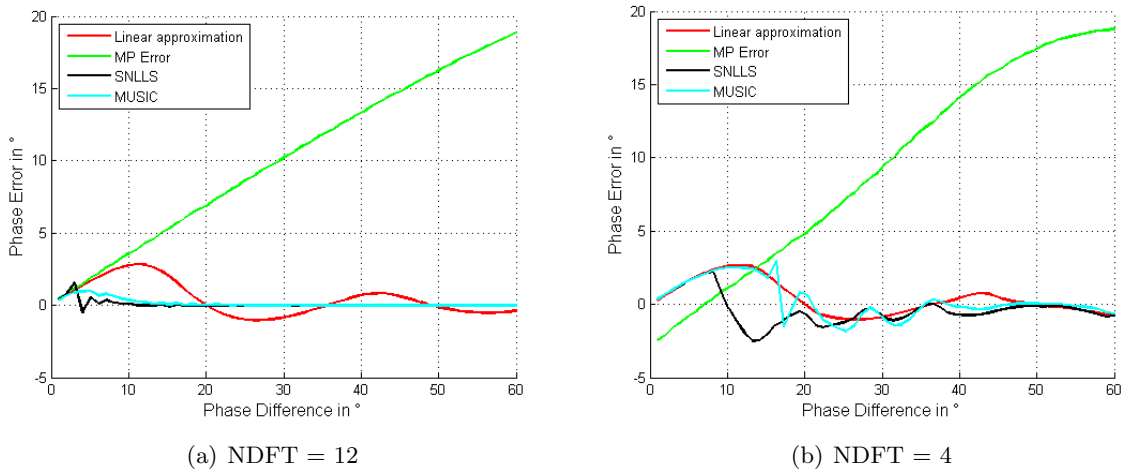


Figure 6.13: Phase Error for MPIC Algorithms - 1 MPC, $f_{mod} = 10:10:100\text{MHz}$, $\text{SNR} = 30\text{dB}$

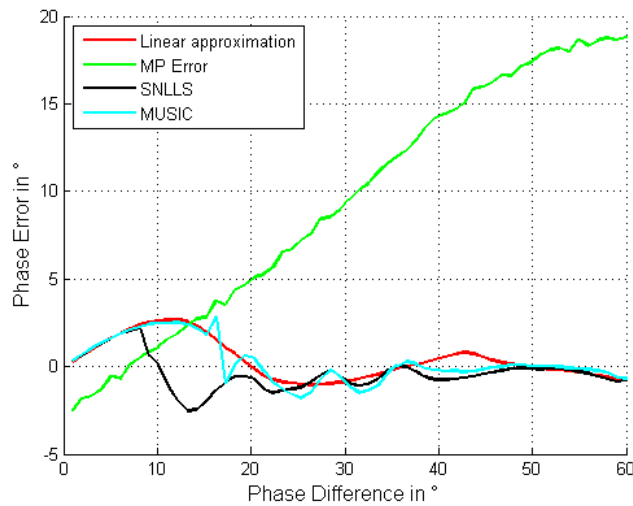


Figure 6.14: Phase Error for MPIC Algorithms - 1 MPC, $\text{NDFT} = 4$, $f_{mod} = 10:10:100\text{MHz}$, $\text{SNR} = 10\text{dB}$

6.3.4 Frequency dependency

All previous results have been run for a maximum frequency of 100MHz and steps of 10MHz. Fig. 6.15 shows the impact of different maximum frequencies. For a reduced maximum frequency (Fig. 6.15(a)) the SNLLS and MUSIC algorithms begin to deteriorate while improving for higher frequencies (Fig. 6.15(b)). A higher maximum frequency also benefits the linear approximation, as a higher frequency includes more periods of the phase error and reduces the residual caused by non-periodic averaging.

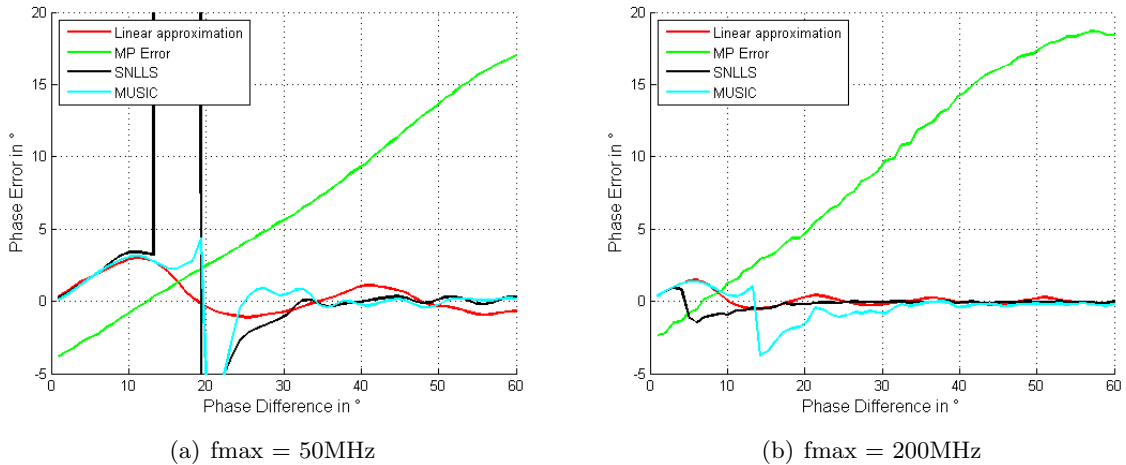


Figure 6.15: Phase Error for MPIC Algorithms - 1 MPC, NDFT = 4, SNR = 30dB

In Fig. 6.16 the maximum frequency is now fixed and the frequency resolution (and with it the number of frequency points) is changed. For a frequency resolution of 1MHz the error of the MUSIC algorithms increases slightly for low phase differences. The linear approximation residual error stays the same for all variations, as the algorithm is not dependent on the number of frequencies used in its calculation, but only on the maximum frequency and the error periods contained in that frequency range.

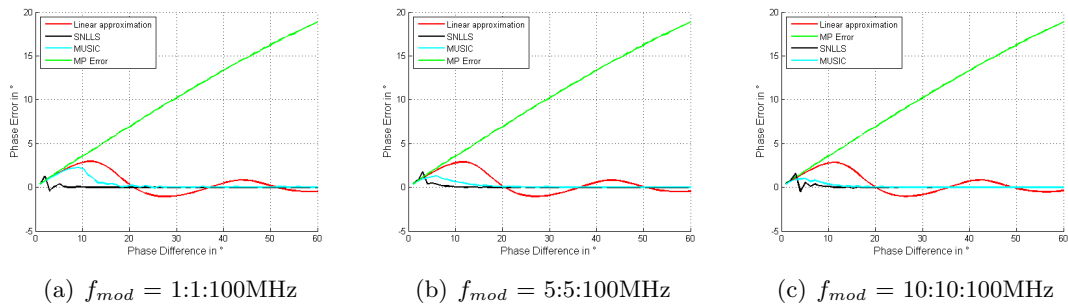


Figure 6.16: Phase Error for MPIC Algorithms with different frequency resolutions - 1 MPC, SNR = 30dB, NDFT = 12.

Decreasing the number of frequency points further (Fig. 6.17) increases the residual error for MUSIC and SNLLS. For small phase differences the residual error of the algorithms even exceed the error of the multipath components. The few points in this case are not enough information for the estimation algorithms to correctly find the MPCs. Especially for the measurement that is also corrupted with wiggling error (Fig. 6.17(b)) the estimation does not improve with larger phase differences. The linear approximation algorithm is again not affected by the low number of frequencies.

Generally higher frequencies are beneficial in reducing MPI. Too few frequency points are problematic for the estimation algorithms, but are no problem for the linear approximation.

6.3.5 Additional MPCs

Fig. 6.18 and Fig. 6.19 show the results for 3 multipath components. The algorithms are able to remove the multipath components as long as the DFT length is large enough (Fig. 6.18(a)) or the maximum frequency is high enough (Fig. 6.19(b)).

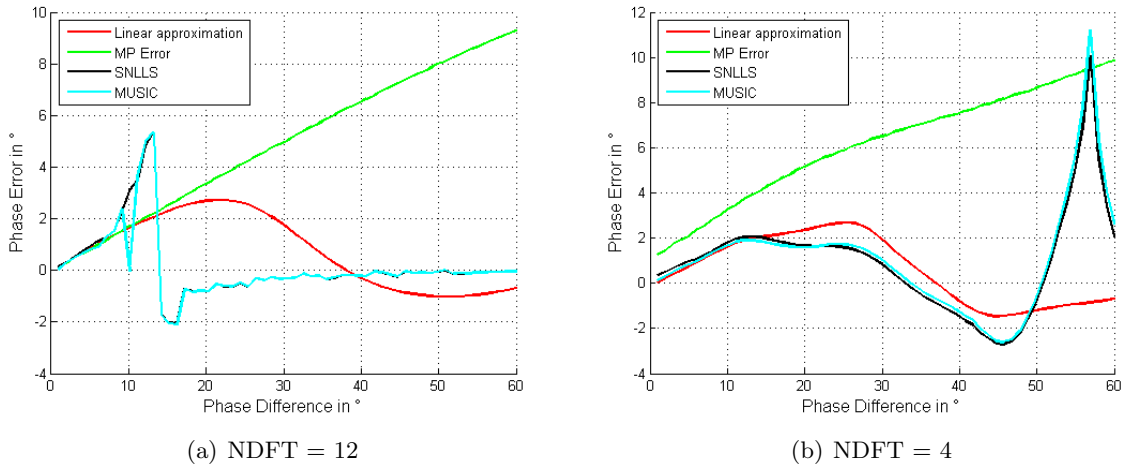


Figure 6.17: Phase Error for MPIC Algorithms - 1 MPC, $f_{mod} = 20:20:100\text{MHz}$, $\text{SNR} = 30\text{dB}$

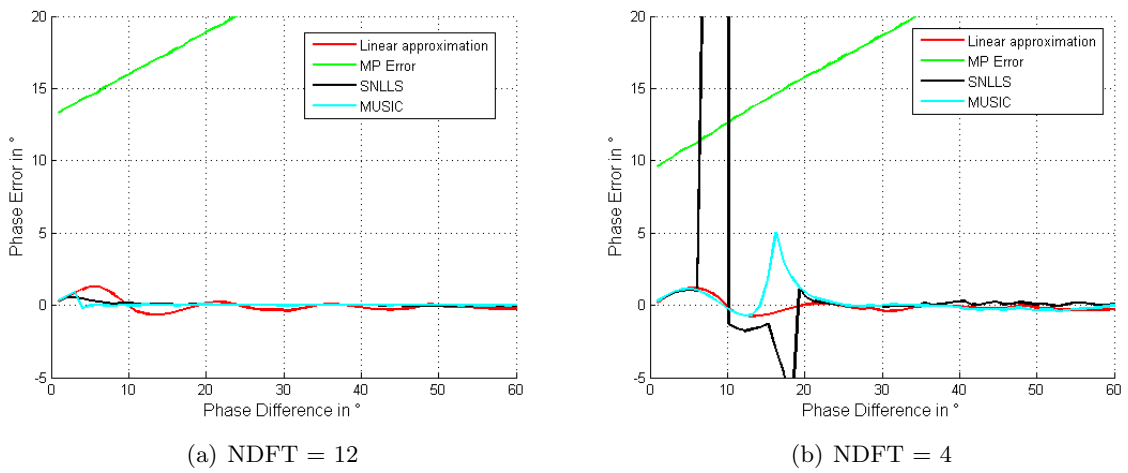


Figure 6.18: Phase Error for MPIC Algorithms - 3 MPC, $f_{mod} = 5:5:100\text{MHz}$, $\text{SNR} = 30\text{dB}$

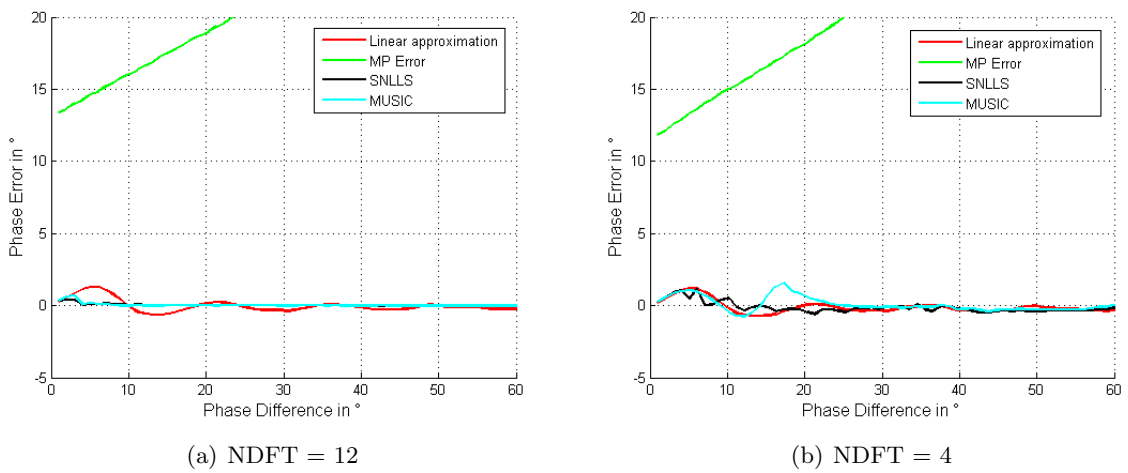


Figure 6.19: Phase Error for MPIC Algorithms - 3 MPC, $f_{mod} = 10:10:200\text{MHz}$, $\text{SNR} = 30\text{dB}$

6.4 MPI in Practice

Following are a few scenarios where the different multipath sources described in Section 4.1 are presented. Generally most multipath effects are present in most images, but only specific ones are highlighted for each point.

6.4.1 Intra-Scene Reflections

The general reflection within a scene is forced by introducing a reflecting object (a box) onto a light surface (a table) and pointing the illumination towards the connection point. The setup is shown with its amplitude image in Fig. 6.20. Also in the amplitude image the reflection onto the table is clearly visible.

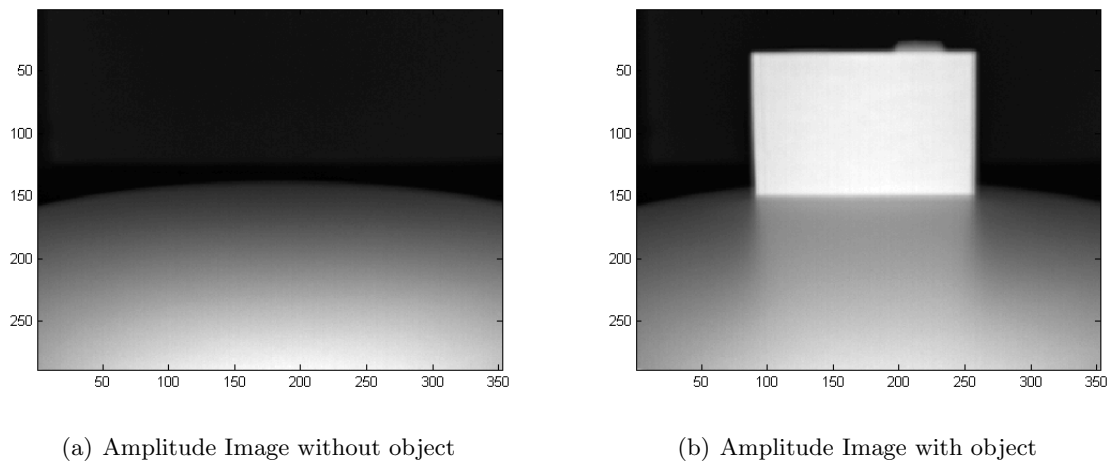


Figure 6.20: Intra-Scene Reflection caused by added bright object

A similar distortion due to the reflection can be seen in the distance image in Fig. 6.21(b), especially if compared to the undisturbed distance in Fig. 6.21(a).

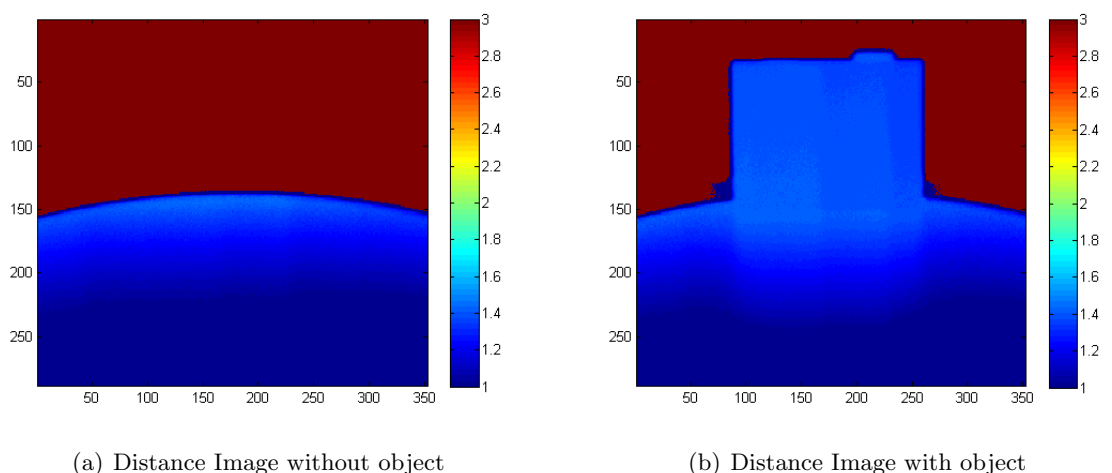


Figure 6.21: Intra-Scene Reflection caused by added bright object

Fig. 6.22 shows a vertical cross-section in the middle of the scene. From left to right it follows first the background wall then diverges into wall and introduced object. The section after around

pixel 150 is again the same surface for both captures. But although the distance of the table was not changed the two images show different distances.

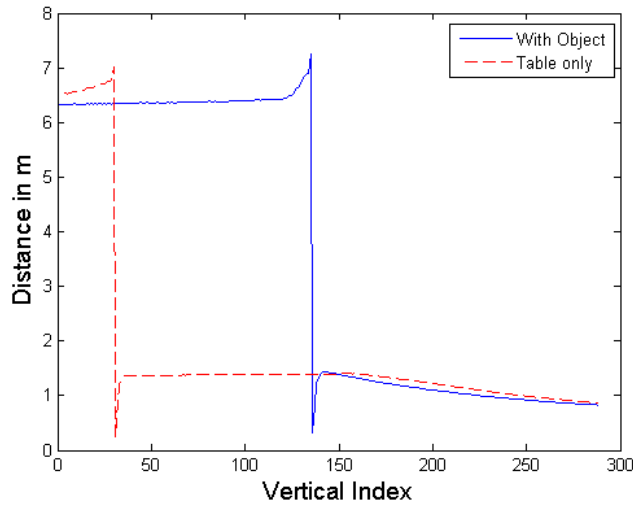


Figure 6.22: Effect of reflection due to introduced object.

The distance difference between the two images at the section of the table is shown in Fig. 6.23. The maximum error is at 12cm which already exceeds 10% of the target distance at this point.

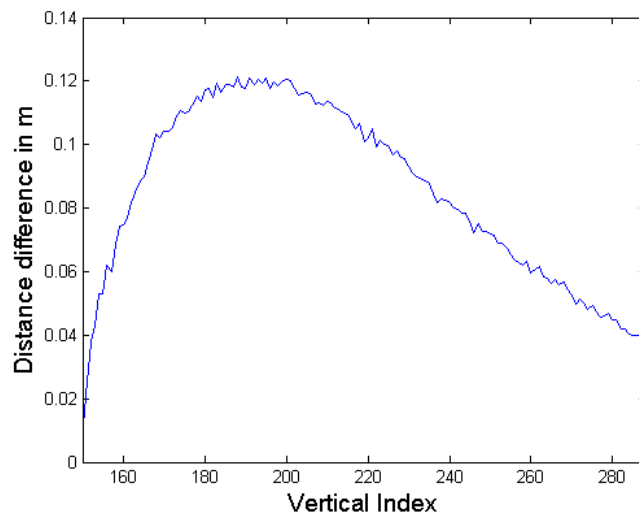


Figure 6.23: Distance error between disturbed and undisturbed image for the table section starting at vertical index 150

6.4.2 Mixed Pixels

A multipath effect that can easily be created in any scene are mixed pixels. Any foreground object will generate mixed pixels along its edges. This is shown on a simple object in front of a plain surface (Fig. 6.24).

In a scatter plot like in Fig. 6.25, the mixed pixel can be easily identified. For further investigations two pixel are chosen as shown in Fig. 6.25(b). For the two pixels at positions (71,141) and (71,156), the phase responses are plotted in Fig. 6.26.

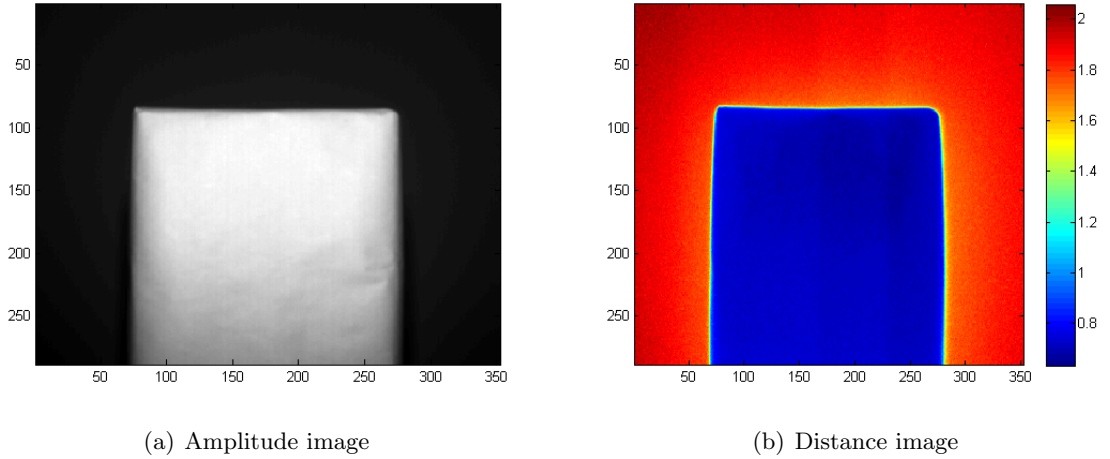


Figure 6.24: Object in front of plain surface for Mixed Pixel observation

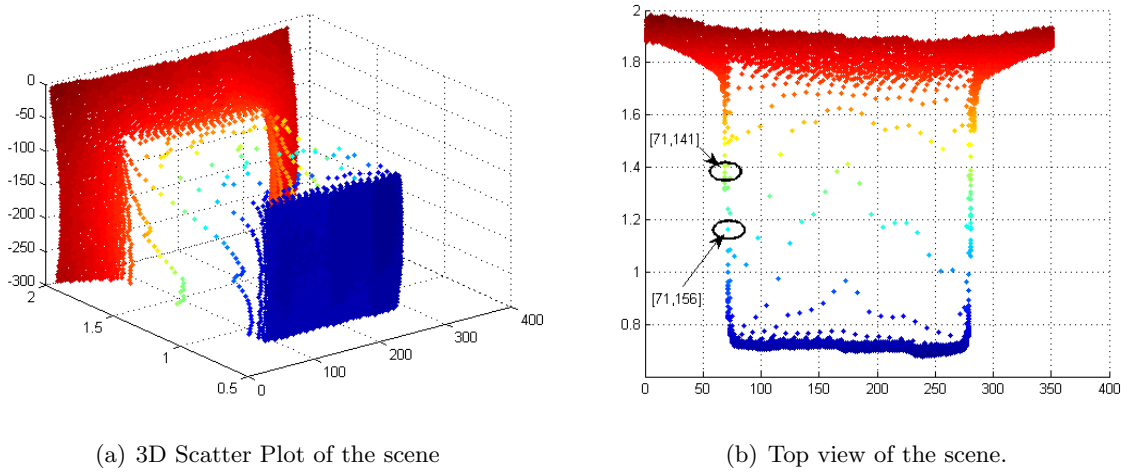


Figure 6.25: Mixed Pixel Positions in 3D image

The two pixel responses have an added trace that fits a theoretical phase error based on the phasor model in (6.1). For the mixed pixels we assume only two dominant components with the near component amplitude set to 1:

$$\varphi(f) = \arg(e^{j \cdot d_1 \cdot \frac{4\pi f}{c}} + a_r \cdot e^{j \cdot d_2 \cdot \frac{4\pi f}{c}})$$

The real distances have been measured as $d_1 = 0.67m$ and $d_2 = 1.87m$. These distances are the same for both mixed pixel. The difference in the phase response is caused by the different relative amplitude of the two components. In Fig. 6.26(a) the pixel is closer to the near distance edge, causing a relative amplitude $a_r < 1$ and the principal component with $d_1 = 0.67m$. For the other pixel in Fig. 6.26(b) the pixel is close to the background, leading to $a_r > 1$ and the principal component with $d_2 = 1.87m$.

While the gradient of the phase response is dependent on the component with higher amplitude, the period of the phase error caused by the other component is the same. As shown in (6.8) the period of the phase error is only dependent on the phase difference of the components, which is the same independent of the stronger component. For the distance difference of 1.2m the phase

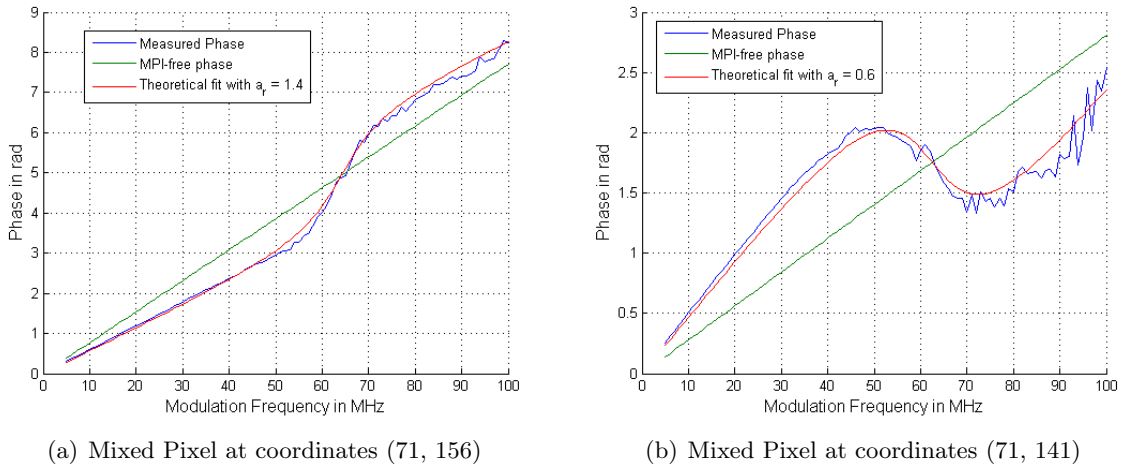


Figure 6.26: Phase response for mixed pixel at 1m20 relative distance and a fitted response based on the known distances.

error period can be calculated as:

$$T = \frac{c}{2 \cdot 1.2m} = 125\text{MHz}$$

The frequency range of the imager is limited to 100MHz, but the zero-crossing on the real phase can be seen close to $\frac{T}{2} = 62.5\text{MHz}$.

Focus

The number of mixed pixel for any edge is also not fixed. Especially focus has an influential role in the width of the edge. In Fig. 6.27 the same scene has been captured using two different settings. In Fig. 6.28(b) the camera optics are set to put the front object into focus, for Fig. 6.28(a) the foreground object has been put out of focus deliberately.

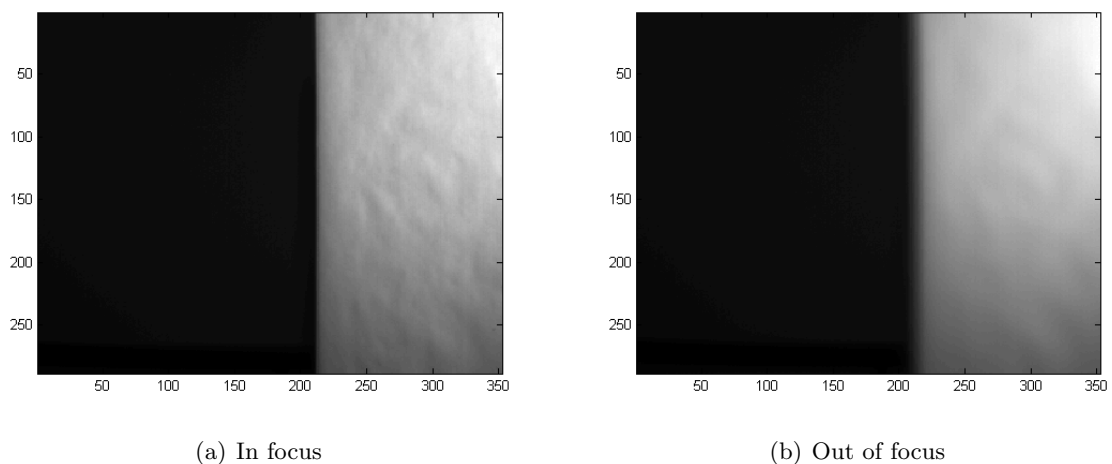


Figure 6.27: Amplitude image of the scene

The distance images are zoomed close to the relevant edge within the image to make the blurry edge more visible.

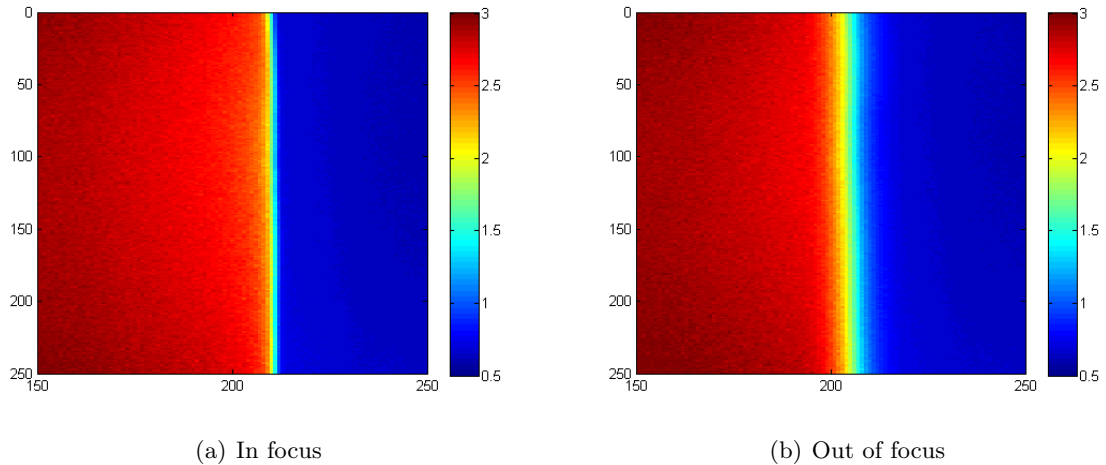


Figure 6.28: Distance images of the scene. Zoomed towards the edge of interest.

Due to the blurred edge for the out-of-focus object the number of pixels with overlapping paths is increased. This can be seen in the comparison of the horizontal cross-sections of the scene in Fig. 6.29.

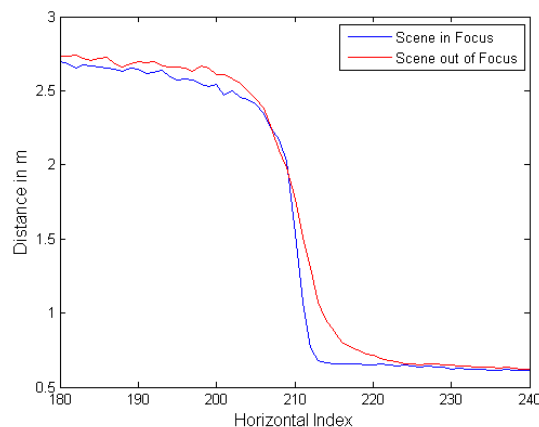


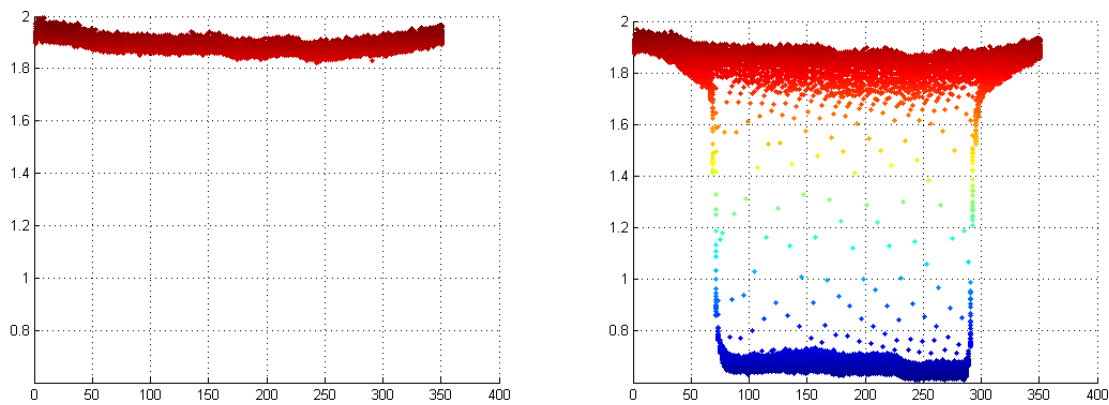
Figure 6.29: Horizontal cross-section of the distance of In-Focus and Out-Of-Focus object.

Therefore to minimize mixed pixels in images, the images should be focused correctly. This might not be possible throughout a whole scene, which means that some section of a scene might suffer from increased occurrence of mixed pixels.

6.4.3 Scattering

Scattering is caused by bright parts of the scene and spread distance error to neighboring pixels. This can be already seen for the setup used for the mixed pixels in Fig. 6.24. For that scene both background only and the scene with the object are captured (Fig. 6.30) and compared. The difference of background and scene including the object is in Fig. 6.31. We can obviously again see flying pixels at the edge of the object. But additionally there is a large trail in distance error on the background level, that extends too far from the distance edge to be explained by simple mixed pixels (and is not visible at the object itself). This is likely scattering from the object to the background.

Fig. 6.32 shows the cross-section of the distance error between background and object. The



(a) Distance of background only.

(b) Distance including an added foreground object

Figure 6.30

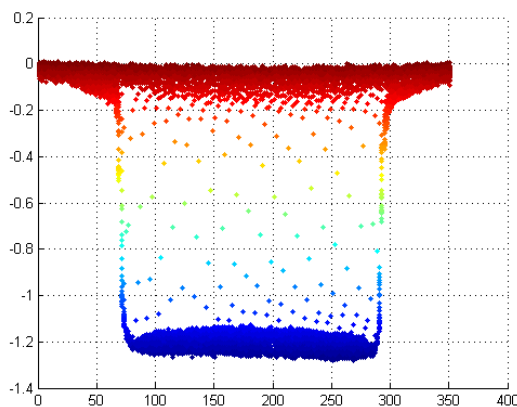


Figure 6.31: Difference of background and scene with introduced object.

object does not show any scattering, while the background has significant distance errors caused by the bright foreground object.

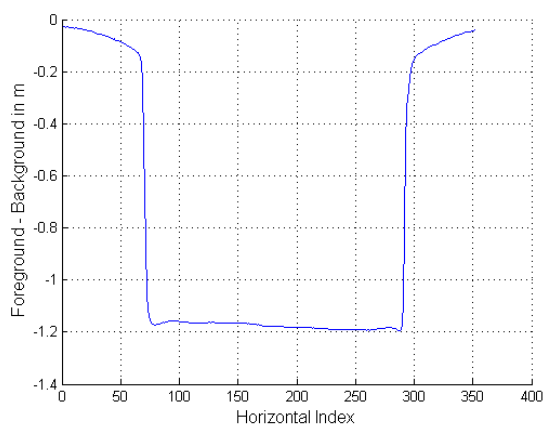


Figure 6.32: Horizontal cross-section of the distance error caused by the foreground object

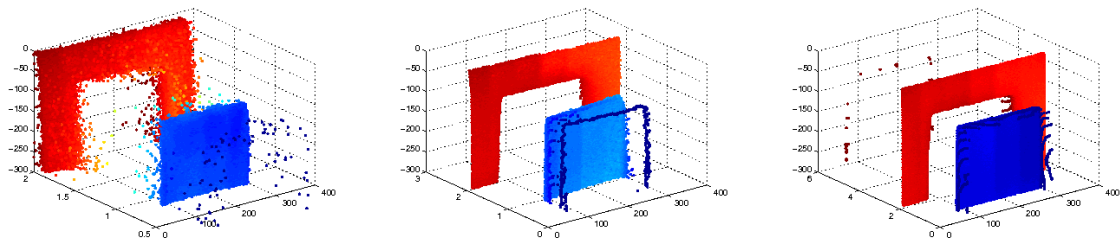
6.5 MPI Compensation

In this section we explore the result of two of the MPI compensation algorithms on real scene captures, specifically MUSIC, as an example for estimation algorithms, and the linear approximation approach.

For this, we go back to the mixed pixel scenario in Fig. 6.24 with a foreground object in the distance difference of 1.2m.

The results for MUSIC for different sets of frequencies are shown in Fig. 6.33 and Fig. 6.34 for 8 and 4 phase measurements respectively. The phases represent the number of equidistant sampling points on the SRF to estimate the distance (identical to the parameter NDFT from previous chapters). For frequencies exceeding 65MHz the ToF sensor only has the option to capture a maximum of 8 phases (12 phases for $f_{max} \leq 65MHz$). All measurements in these figures are done up to 100MHz modulation frequency with different frequency resolution. The resolution is noted as Δf and is the size of the equidistant steps from Δf to f_{max} with a minimum frequency of 10MHz.

Contrary to the simulation results in Fig. 6.16, the measurement results for the most frequency points (1MHz resolution) show a significantly worse performance. For the higher DFT resolution and high frequency resolution the result is very noisy (Fig. 6.33(a)). This is caused by an incorrect choice of frequencies. The MUSIC algorithm requires the results at equidistant frequency points from Δf to f_{max} . For a resolution of 1MHz the minimum frequency needed to be at 1MHz, but data is only available starting at 10MHz. With this the estimation for this resolution is not correct. The results for 10MHz and 25MHz resolution show that the mixed pixels have been successfully removed. In Fig. 6.33(b) there are considerable artifacts at the edge of the object. These artifacts are less pronounced for the variant with only 4 frequency points at 25MHz distance. For these frequencies though, there are some pixels far away from the scene, which were calculated at negative distances in front the object and were mirrored into the background of the image.

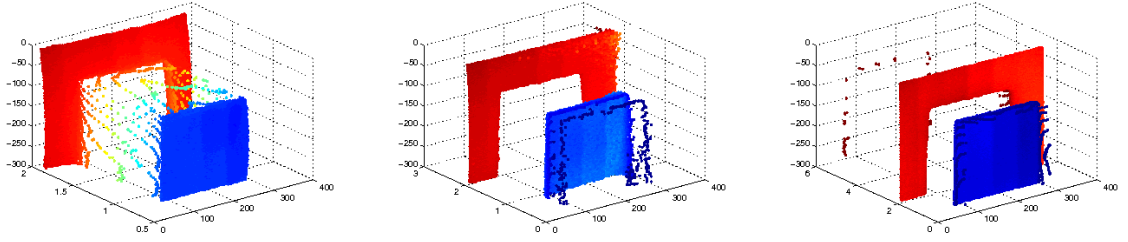


(a) $f_{max} = 100MHz$, $\Delta f = 1MHz$ (b) $f_{max} = 100MHz$, $\Delta f = 10MHz$ (c) $f_{max} = 100MHz$, $\Delta f = 25MHz$

Figure 6.33: Multipath Compensation using MUSIC for various frequency settings with 8 phase measurement. Object in 1.2m relative distance to background.

Using only a 4-phase measurement the results show worse performance. The results for 25MHz resolution show again mirrored pixel in the background, but has overall less pixel artifacts. The performance is slightly worse for a 10MHz resolution (Fig. 6.34(b)) and shows very little actual compensation effect for 1MHz resolution in Fig. 6.34(a), again caused by an incorrect frequency range. Worse behavior for 4-phase measurements compared to 8-phase measurements was already shown in the simulation in Section 6.3.3.

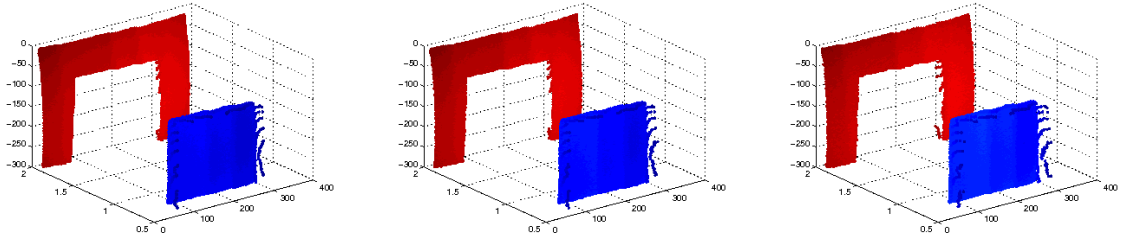
Using a simple linear approximation approach, the resulting depth images are shown in Fig. 6.35 and Fig. 6.36. The frequency resolution and the number of phases used in the calculation show little to no influence on the results. There are again artifacts visible at the edges of the object similar to the result of the MUSIC algorithm. The resulting distance images also show no



(a) $f_{max} = 100\text{MHz}$, $\Delta f = 1\text{MHz}$ (b) $f_{max} = 100\text{MHz}$, $\Delta f = 10\text{MHz}$ (c) $f_{max} = 100\text{MHz}$, $\Delta f = 25\text{MHz}$

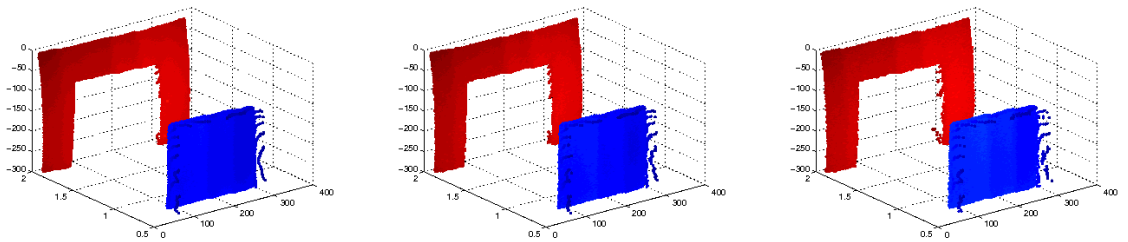
Figure 6.34: Multipath compensation using MUSIC for various frequency settings with 4 phase measurement. Object in 1.2m relative distance to background.

significant increase in noise, in contrast to Fig. 6.33(a). The linear approximation does not require equidistant frequencies as its input, therefore the results for 1MHz resolution are valid.



(a) $f_{max} = 100\text{MHz}$, $\Delta f = 1\text{MHz}$ (b) $f_{max} = 100\text{MHz}$, $\Delta f = 10\text{MHz}$ (c) $f_{max} = 100\text{MHz}$, $\Delta f = 25\text{MHz}$

Figure 6.35: Multipath compensation using linear approximation for various frequency settings with 8 phase measurement. Object in 1.2m relative distance to background.



(a) $f_{max} = 100\text{MHz}$, $\Delta f = 1\text{MHz}$ (b) $f_{max} = 100\text{MHz}$, $\Delta f = 10\text{MHz}$ (c) $f_{max} = 100\text{MHz}$, $\Delta f = 25\text{MHz}$

Figure 6.36: Multipath compensation using linear approximation for various frequency settings with 4 phase measurement. Object in 1.2m relative distance to background.

6.5.1 Choosing the correct frequency

As shown in Section 6.4.2 the mixed pixels have a periodic distance error where the period is dependent on the distance of foreground object to the background (Fig. 6.26). For this scene the distance is approximately 1.2m and with (6.8) this results in a period of 125MHz. Assuming no other significant multipath components this corresponds to a zero-crossing of the distance error at 62.5MHz.

Fig. 6.37 shows the scene capture at 63MHz modulation frequency. At this frequency the distance error caused by multipath (specifically by multipath difference of 1.2m) should be close to zero. This is indeed the case, aside from a few outliers.

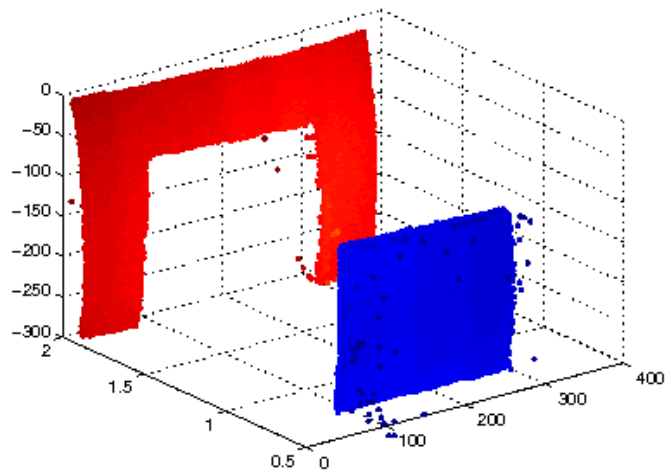


Figure 6.37: Scene capture of foreground object in 1.2m relative distance at 63MHz modulation frequency.

Fig. 6.38 and Fig. 6.39 show the horizontal cross-sections of the scene image at 63MHz in Fig. 6.37 and the compensation results at the various frequency resolutions. The distance estimate at 63MHz is supposedly the true distance, as the multipath error should be close to zero.

For the MUSIC algorithm (Fig. 6.38) the distance estimate of the foreground object is closest to the true distance for a frequency resolution of 25MHz. Therefore the lowest frequency resolution setting is the best both in terms of outliers and absolute distance estimate.

The linear approximation estimate in Fig. 6.39 is similar across all frequency resolutions. The estimate shows an error over all resolutions that is higher than the best-case error for MUSIC. This is consistent with the simulations that showed that the linear approximation has a residual error if not calculated over full error periods. A full error period cannot be used as the maximum frequency is limited to 100MHz.

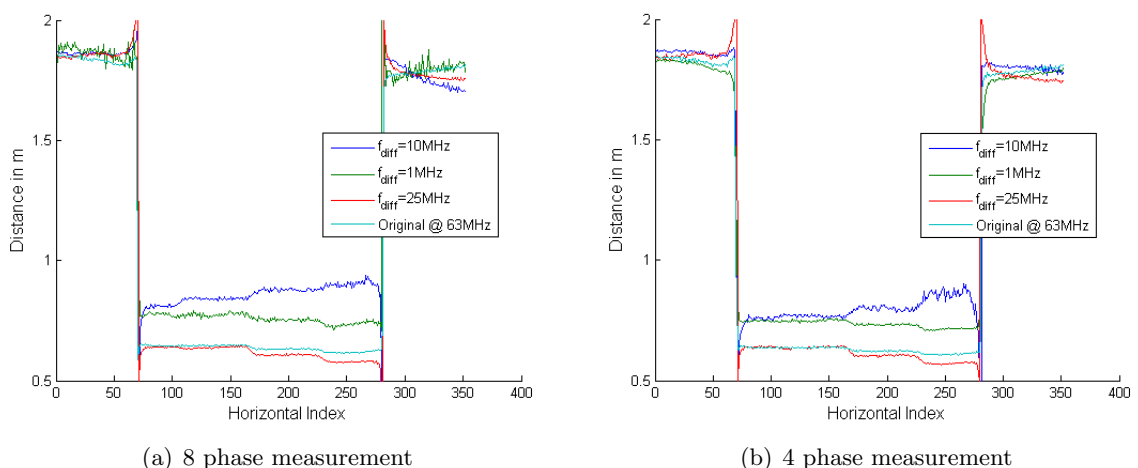


Figure 6.38: Horizontal cross-sections of the distance for the image capture at 63MHz and the distance estimate of MUSIC for different frequency resolutions.

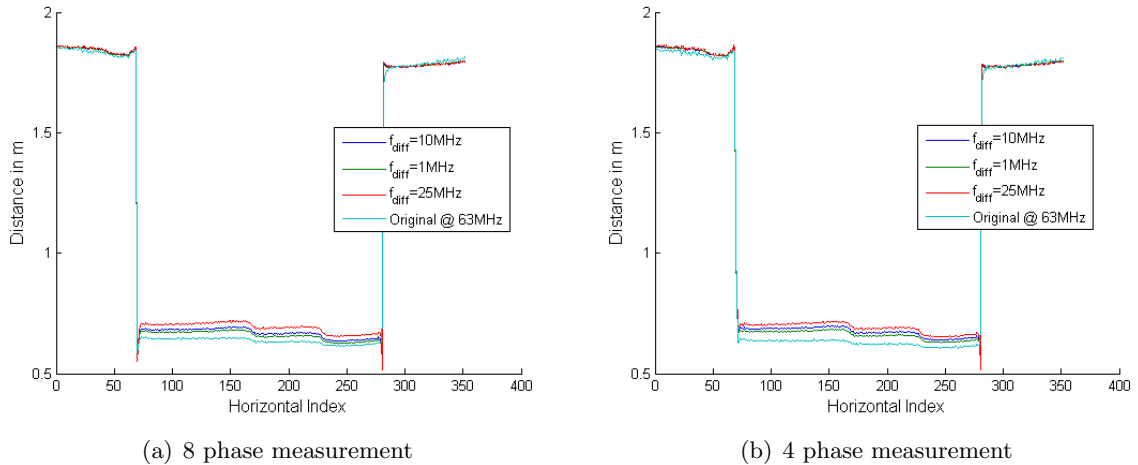


Figure 6.39: Horizontal cross-sections of the distance for the image capture at 63MHz and the distance estimate of linear approximation for different frequency resolutions.

As just shown, the ideal frequency is the zero-crossing of the periodic phase error in the mixed pixel phase return. For the linear approximation method the averaging should ideally be done over a whole error period. This cannot be achieved for this scene, as the period is 125MHz and the maximum modulation frequency is below that. With that in mind, if the maximum frequency is lower than even the half-period of 62.5MHz the linear approximation is expected to no longer work.

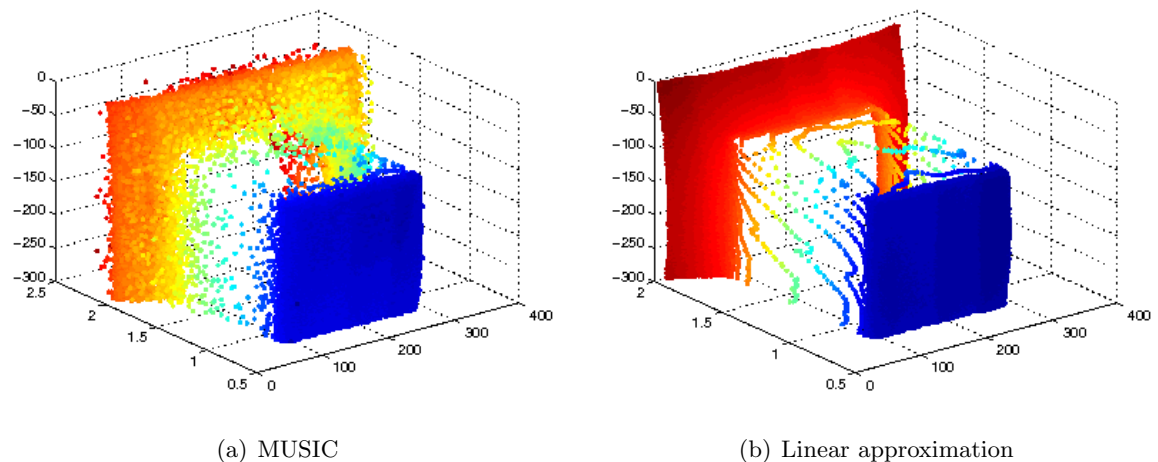


Figure 6.40: Multipath compensation with a maximum frequency of 40MHz with 8-phase measurement.

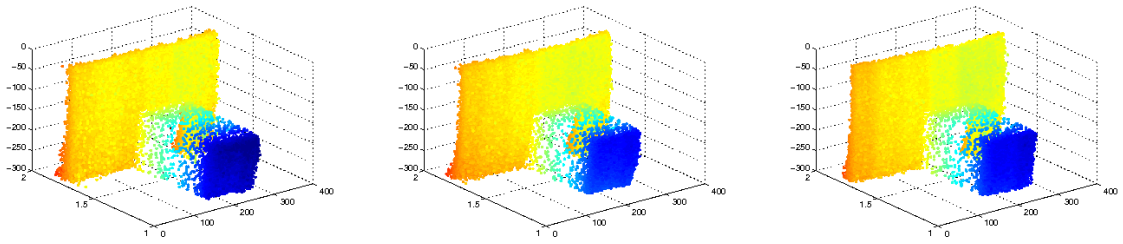
This is shown in Fig. 6.40(b) with a maximum modulation frequency of 40MHz. Not only the linear regression, but also the MUSIC algorithm can no longer compensate the mixed pixels (Fig. 6.40(a)).

6.5.2 Mixed Pixels with insufficient distance

The distance of the object relative to the background causes similar problems as does low maximum frequency. For small distances the period of the error in the frequency domain increases and higher modulation frequencies are needed to cover this period. Fig. 6.41 and Fig. 6.42 show the result in MPI compensation for MUSIC and linear approximation for a target

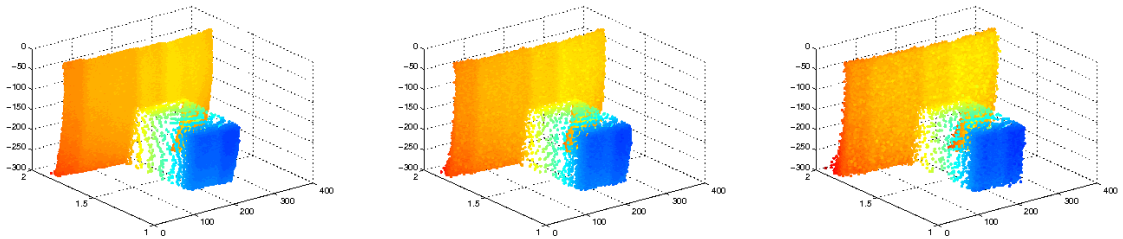
at half the relative distance to the background. For this the period of the phase error increases to 250MHz, well above the maximum possible modulation frequency.

This again causes both MUSIC and the linear approximation approach to not be able to resolve the mixed pixels in the scene, independent of the resolution of the frequency used.



(a) $f_{max} = 100\text{MHz}$, $\Delta f = 1\text{MHz}$ (b) $f_{max} = 100\text{MHz}$, $\Delta f = 10\text{MHz}$ (c) $f_{max} = 100\text{MHz}$, $\Delta f = 25\text{MHz}$

Figure 6.41: Multipath compensation using MUSIC for various frequency settings with 8 phase measurement. Object in 0.6m relative distance to background.



(a) 10:1:100MHz

(b) 10:10:100MHz

(c) 25:25:100MHz

Figure 6.42: Multipath compensation using linear approximation for various frequency settings with 8 phase measurement. Object in 0.6m relative distance to background.

Conclusion

This final chapter concludes the thesis. It reflects on the topics presented throughout this thesis in Section 7.1 and ends with further possible areas of interest in Section 7.2.

7.1 Summary

7.1.1 Multipath Error

Interference from multipath components has been shown to be possibly significant, but is completely dependent on the scene configuration and can therefore not be addressed by calibration efforts. The different possibilities for multiple returns are generally all present in all images.

The possible impact of the multipath returns has been shown with simulations on a simple model. The occurrence of different multipath effects has also been shown in real depth images taken with a state-of-the-art ToF camera.

Especially dominant and unavoidable multipath errors occur at transitions from foreground objects to a background, called mixed or flying pixels. Other sources like in-scene reflections and scattering are less prominent. It was also shown that an AMCW ToF system is generally unable to deal with multipath interference in its normal operation mode as the limited spectral contents of the single-frequency periodic reference signal does not allow for a reconstruction of the individual MPCs.

7.1.2 Multipath Compensation

The compensation of the multipath related error is possible but difficult for AMCW ToF. Existing approaches include a model based calculation and a change of the reference signal away from AMCW signals with e.g. modulation coding.

A close look was taken on multi-frequency methods. Interpreting the problem of identifying the MPCs as a correlative channel sounding problem, the multi-frequency approach basically implements a discrete frequency sweep of the input signal using multiple image captures. This results in a periodic phase error over frequency depending on the phase difference of the multipath component.

The results from the different frequency measurements then can be used in various algorithms. This thesis shows the general applicability of Non-Linear Least Squares estimation and spectral estimation theory. Specifically used for simulation was a separable non-linear least squares and MUSIC respectively. Also implemented was a simple Linear Approximation algorithm in contrast to the more complex estimation approaches.

Simulation on these algorithms with the multipath model have shown that the non-linear estimation as well as the spectral estimation are able to achieve similarly good performance on two or more MPCs. The linear approximation approach can also reduce the multipath error considerably, but suffers from a systematic residual error if not calculated over a full period of the multipath phase error.

The following has also been shown:

- all methods are not able to reliably identify MPCs that are too small
- quality of the results for all methods increases with higher maximum modulation frequency
- all methods are robust against white noise (but the residual error increases for the estimation algorithms in case of non-white noise sources, e.g. wiggling error)

Practical results

The algorithms for MUSIC and Linear Approximation have been executed on real distance data images contaminated with mixed pixel. Both algorithms are able to identify and remove the mixed pixels if the distance between the objects is high enough and the frequency range is sufficient. As shown in simulation, a too small multipath phase difference (distance difference for mixed pixels) is problematic for all algorithms.

The linear approximation has several advantages compared to MUSIC:

- similar results for mixed pixel compensation
- fast and easy calculation
- no prerequisites on frequency selection (MUSIC requires uniformly spread frequencies)

Linear Approximation therefore would be a simple solution for mixed pixel compensation if the other multipath components are not required (are not recovered with this approach).

7.2 Outlook

This thesis only qualitatively investigated the different solutions for multipath compensation as it was not possible to build a setup that allowed for accurate base distance measurements or calibration. A more accurate measurement setup would allow to measure the actual residual errors of the different compensation methods.

Of even more interest would be the investigation of coded modulation schemes as they allow for relatively complex illumination sequences for special scenarios and applications.

Bibliography

- [1] S. Fuchs, “Multipath interference compensation in time-of-flight camera images,” in *Pattern Recognition (ICPR), 2010 20th International Conference on*. IEEE, 2010, pp. 3583–3586.
- [2] D. Jiménez, D. Pizarro, M. Mazo, and S. Palazuelos, “Modeling and correction of multipath interference in time of flight cameras,” *Image and Vision Computing*, vol. 32, no. 1, pp. 1–13, 2014.
- [3] J. P. Godbaz, M. J. Cree, and A. A. Dorrington, “Closed-form inverses for the mixed pixel/multipath interference problem in amcw lidar,” in *IS&T/SPIE Electronic Imaging*. International Society for Optics and Photonics, 2012, pp. 829 618–829 618.
- [4] A. Bhandari, A. Kadambi, R. Whyte, C. Barsi, M. Feigin, A. Dorrington, and R. Raskar, “Resolving multipath interference in time-of-flight imaging via modulation frequency diversity and sparse regularization,” *Opt. Lett.*, vol. 39, no. 6, pp. 1705–1708, Mar 2014. [Online]. Available: <http://ol.osa.org/abstract.cfm?URI=ol-39-6-1705>
- [5] A. Kadambi, R. Whyte, A. Bhandari, L. Streeter, C. Barsi, A. Dorrington, and R. Raskar, “Coded time of flight cameras: sparse deconvolution to address multipath interference and recover time profiles,” *ACM Transactions on Graphics (TOG)*, vol. 32, no. 6, p. 167, 2013.
- [6] S. Fuchs and S. May, “Calibration and registration for precise surface reconstruction with time-of-flight cameras,” *International Journal of Intelligent Systems Technologies and Applications*, vol. 5, no. 3-4, pp. 274–284, 2008.
- [7] D. Piatti, F. Remondino, and D. Stoppa, “State-of-the-art of tof range-imaging sensors,” in *TOF Range-Imaging Cameras*. Springer, 2013, pp. 1–9.
- [8] E. Charbon, M. Fishburn, R. Walker, R. K. Henderson, and C. Niclass, “Spad-based sensors,” in *TOF Range-Imaging Cameras*. Springer, 2013, pp. 11–38.
- [9] R. Schwarte, Z. Xu, H.-G. Heinol, J. Olk, R. Klein, B. Buxbaum, H. Fischer, and J. Schulte, “New electro-optical mixing and correlating sensor: facilities and applications of the photonic mixer device (pmd),” in *Lasers and Optics in Manufacturing III*. International Society for Optics and Photonics, 1997, pp. 245–253.
- [10] R. Lange and P. Seitz, “Solid-state time-of-flight range camera,” *Quantum Electronics, IEEE Journal of*, vol. 37, no. 3, pp. 390–397, 2001.
- [11] H. Rapp, “Experimental and theoretical investigation of correlating tof-camera systems,” Master’s thesis, 2007.
- [12] M. Lindner and A. Kolb, “Calibration of the intensity-related distance error of the pmd tof-camera,” in *Intelligent Robots and Computer Vision XXV: Algorithms, Techniques, and Active Vision*, vol. 6764. International Society for Optics and Photonics, 2007, p. 67640W.
- [13] D.-I. D.-B. B. S. Fuchs, “Calibration and multipath mitigation for increased accuracy of time-of-flight camera measurements in robotic applications,” 2012.

- [14] L. Pancheri and D. Stoppa, “Sensors based on in-pixel photo-mixing devices,” in *TOF Range-Imaging Cameras*. Springer, 2013, pp. 69–89.
- [15] J. Grünwald, “Investigation of systematic errors in time-of-flight imaging,” Master’s thesis, University of Technology Graz, Austria, 2013.
- [16] T. Kavli, T. Kirkhus, J. T. Thielemann, and B. Jagielski, “Modelling and compensating measurement errors caused by scattering in time-of-flight cameras,” in *Two-and Three-Dimensional Methods for Inspection and Metrology VI*, vol. 7066. International Society for Optics and Photonics, 2008, p. 706604.
- [17] J. Mure-Dubois and H. Hügli, “Real-time scattering compensation for time-of-flight camera,” in *Proceedings of the ICVS Workshop on Camera Calibration Methods for Computer Vision Systems*, 2007.
- [18] S. A. Gudmundsson, H. Aanæs, and R. Larsen, “Environmental effects on measurement uncertainties of time-of-flight cameras,” in *Signals, Circuits and Systems, 2007. ISSCS 2007. International Symposium on*, vol. 1. IEEE, 2007, pp. 1–4.
- [19] A. A. Dorrington, J. P. Godbaz, M. J. Cree, A. D. Payne, and L. V. Streeter, “Separating true range measurements from multi-path and scattering interference in commercial range cameras,” in *IS&T/SPIE Electronic Imaging*. International Society for Optics and Photonics, 2011, pp. 786 404–786 404.
- [20] J. P. Godbaz, M. J. Cree, and A. A. Dorrington, “Mixed pixel return separation for a full-field ranger,” in *Image and Vision Computing New Zealand, 2008. IVCNZ 2008. 23rd International Conference*. IEEE, 2008, pp. 1–6.
- [21] J. P. Godbaz, A. A. Dorrington, and M. J. Cree, “Understanding and ameliorating mixed pixels and multipath interference in amcw lidar,” in *TOF Range-Imaging Cameras*. Springer, 2013, pp. 91–116.
- [22] A. F. Molisch, *Wireless communications*. Wiley.com, 2010, vol. 15.
- [23] G. Golub and V. Pereyra, “Separable nonlinear least squares: the variable projection method and its applications,” *Inverse problems*, vol. 19, no. 2, p. R1, 2003.
- [24] P. Stoica and R. L. Moses, *Introduction to spectral analysis*. Prentice hall Upper Saddle River, NJ, 1997, vol. 1.
- [25] M. L. Simpson, M.-D. Cheng, T. Q. Dam, K. E. Lenox, J. R. Price, J. M. Storey, E. A. Wachter, and W. G. Fisher, “Intensity-modulated, stepped frequency cw lidar for distributed aerosol and hard target measurements,” *Applied optics*, vol. 44, no. 33, pp. 7210–7217, 2005.
- [26] A. Kirmani, A. Benedetti, and P. A. Chou, “Spumic: Simultaneous phase unwrapping and multipath interference cancellation in time-of-flight cameras using spectral methods,” in *Multimedia and Expo (ICME), 2013 IEEE International Conference on*. IEEE, 2013, pp. 1–6.